

Passive Battery Thermal Management in Electric Vehicles using Fin Embedded Composite Phase Change Materials

A thesis
Submitted in fulfilment
of the requirement for the degree

of

**Masters by Research and Thesis (Centre of Research and Enterprise
in Engineering, engCORE)**

at

The Institute of Technology, Carlow

by

Foo Shen Hwang

Supervisor:

Dr Thomas Confrey & Dr Stephen Scully




Year of submission

2021

DECLARATION OF ORIGINALITY

“I hereby declare that this thesis entitled “Passive Battery Thermal Management in Electric Vehicles using Fin Embedded Composite Phase Change Materials” is my own work, except where I have received help as stated in the acknowledgement. All quotations and summary of the work of others have been acknowledged where appropriate. Permission is granted for this work to be copied in whole or in part for private study, provided that in each case the user acknowledges the source and his or her indebtedness to the author.

Foo Shen Hwang

Signed:  _____

Date : 14/01/21

Abstract

The efficiency of battery packs installed in electric vehicles (EVs) is greatly influenced by their operating temperature. Thus, it is paramount that an effective battery thermal management system be incorporated. While there are numerous existing battery thermal management systems out in the current market such as air, liquid, and refrigerant cooling systems, they require additional energy inputs. A novel solution to this predicament is through passive thermal management systems using phase change materials (PCMs) as a cooling medium. PCMs can absorb large quantities of heat passively and are able to regenerate themselves as they cool. The study conducted aims at designing a passive thermal management system that utilizes such PCMs for the purpose of regulating battery temperatures in EVs to improve their performance.

The investigation first focused on designing a passive PCM thermal management system that would be able to house a standard 18650 battery, conduct heat away from the battery to the PCM material, enhance the thermal conductivity of the PCM, be structurally strong and conform to a honeycomb structure to minimize space wastage. PCM Rubitherm RT27, a type of paraffin, was selected as the PCM component for its high latent heat capacity and melting point of 27°C which is within the optimum temperature range of a lithium-ion battery. Upon conceptualizing an initial design to fit the aforementioned requirements, the design was then further optimized through computational fluid dynamics (CFD) based on the heat generated by the battery at varying discharge rates. The structure was further parametrized with the ideal of reducing its overall volume and weight while at the same time reducing the battery's maximum temperature as it goes through varying discharge rates. The final design was then simulated under varying ambient temperatures to determine its performance at various climates.

The final design for the PCM thermal management system was determined to be an aluminium finned hexagonal structure with a circular core that utilizes RT27 as a PCM medium as it fulfils the criteria set. After further optimizing the structure with CFD, it was determined that a model with a width length of 35.0 mm and 10 internal fins had the greatest effect in lowering the battery's maximum temperature throughout varying discharge rates. It was also deduced that the prototype can perform well when ambient temperatures are between 15°C-27°C which is sufficient for equatorial climates. Hotter weather would reduce the efficiency of the prototype. Future works on the prototype could potentially improve upon its performance for pack level design and analyse its manufacturability.

Acknowledgement

The success of this project is attributed to several parties. The utmost gratitude is given to my supervisor, Thomas Confrey, who dedicated his time in providing guidance and direction for this investigation, as well as assisting me in revising several iterations of my paper and sourcing for both equipment and materials for the project. Without his assistance, this project would not have been successful. Additionally, I would like to thank Barrey Flannery from Xerotech for providing additional batteries for the project. Further gratitude is given to Dean Callaghan, Cathal Nolan, Darren Kavanagh, Stephen Scully and Andrew Keppel for sharing their knowledge and expertise with respect to the project. I would also like to further thank the Institute of Technology Carlow for awarding the President's scholarship, which contributed financially to the project. And finally, I would like to express my heartfelt appreciation to the friends and family who have supported me throughout this entire journey.

Table of Contents

Abstract	2
Acknowledgement	3
Table of Contents	4
Glossary	6
Abbreviations	9
Formula symbols	10
1. Introduction	1
1.1 Market Demand for EVs	1
1.2 Significance of Battery Thermal Management (BTM) System	4
1.2.1 Low Temperature Effects	5
1.2.2 High Temperature Effects	7
1.3 Project Scope and Vision	9
2. Literature Review	11
2.1 Current BTM Systems	11
2.1.1 Air-Based	11
2.1.2 Liquid-Based	13
2.1.2.1 Indirect Liquid Cooling	14
2.1.2.2 Immersion Cooling	16
2.1.3 Refrigerant-Based Cooling	16
2.1.4 Comparison Between the Various Cooling Systems	18
2.2 PCM Thermal Management	20
2.2.1 Inorganic PCMs	21
2.2.2 Organic PCMs	22
2.2.3 Comparison of Inorganic and Organic PCMs	23
2.2.4 PCM Encapsulation and Thermal Conductivity Enhancement	26
3. Methodology	29
3.1 Design concept	29
3.2 CFD method	35
3.2.1 Lithium-Ion Heat Generation Model	35
3.2.2 PCM thermophysical characteristics and modelling	36
3.2.3 Structure optimization of the final PCM model	40

4.	Results: Battery Thermal Characteristics	41
4.1	Function type and battery heat generation CFD settings	41
4.1.1	Polynomial function	41
4.1.2	Exponential function	42
4.1.3	Power function	42
4.1.4	Root mean square error	43
4.1.5	Battery heat generation CFD settings	43
4.2	Heat generation function	46
4.2.1	Polynomial function	46
4.2.2	Exponential function	47
4.2.3	Power function	48
4.3	RMSE values	50
4.4	Comparison of battery heat generation CFD results	53
5.	Results: PCM Thermal Management System	56
5.1	Prototype Design	56
5.2	Structure Parameterization	59
5.2.1	Model Width Parameterization	59
5.2.2	Fin Number Parameterization	63
5.2.3	Comparison of the system with/without PCM	66
5.2.4	Varying ambient temperature	67
5.3	Final prototype design	72
5.4	Future works and recommendations	74
6.	Conclusion	75
7.	References	77
8.	Bibliography	88
9.	Appendices	89

Glossary

Battery Thermal Management (BTM)

General term used to describe all the operational components that regulate the temperature of the battery pack, either through cooling or heating-based systems.

Computational Fluid Dynamics (CFD)

Subset of fluid mechanics that utilizes data structures and numerical analyses to model and simulate problems relating to fluid flows.

Computer Numerated Control (CNC)

CNC machining is a form of subtractive manufacturing that removes material from a block, such as with metals or plastics, with motorised machine tools to form a finished geometry.

Direct Metal Laser Sintering (DMLS)

Type of 3D printing process that melts/fuses powdered metals to form multiple layers. The cumulation of these layers ultimately form the main body of the part to be manufactured.

Electric Vehicle (EV)

Vehicle that is propelled by an induction-based motor with battery packs as its main power source.

Heating Ventilation Air Conditioning (HVAC)

HVAC in the context of automobiles refers to the subsection of the vehicle that cools or heats air circulating in the cabin.

Internal Combustion Engine Vehicle (ICEV)

Vehicle that utilizes an internal combustion engine for its propulsion with carbon-based fuel as its energy source.

Latent Heat (LH)

The energy absorbed/released by an object or thermodynamic system during a constant temperature process.

Mean Absolute Error (MAE)

Measure of errors across a dataset by averaging of its error values.

Mean Absolute Percentage Error (MAPE)

Measure of errors across a dataset by averaging the percentage error values.

Phase Change Material (PCM)

Substance that has high latent heat capacity which can store large quantities of thermal energy at phase transition. The material absorbs heat as the material melts and disperses heat as it solidifies, allowing for stable temperature regulation.

Root Mean Square Error (RMSE)

Measure of errors across a dataset by squaring error values before averaging them and taking the square root of the result.

Sensible Heat (SH)

The heat transferred to an object or system without causing a phase change.

State of Charge (SOC)

In the context of batteries, State of Charge refers to the usable battery capacity remaining across the battery throughout its transient charge and discharge cycles.

Subcooling (SC)

A substance that exists in its liquid state below its normal boiling point.

Thermal Runaway (TR)

Self-accelerating reaction caused by excessive additional heat from exothermic reactions. The gradual build-up of heat is not dispersed, leading to an exponential rise in temperature, which would in turn eventually trigger an explosion.

User Defined Function (UDF)

Function developed by a user in a program or environment that has pre-existing functions.

Abbreviations

ANSYS	Analysis System Software
BTM	Battery Thermal Management
CFD	Computational Fluid Dynamics
CNC	Computer Numerated Control
DMLS	Direct Metal Laser Sintering
EV	Electric Vehicle
HVAC	Heating Ventilation Air-Conditioning
ICEV	Internal Combustion Engine Vehicle
MAE	Mean Absolute Error
MAPE	Mean Absolute Percentage Error
PCM	Phase Change Material
RMSE	Root Mean Square Error
SOC	State of Charge
TR	Thermal Runaway
UDF	User Defined Function

Formula symbols

c_p	Specific heat capacity ($\frac{J}{kg K}$)
h	Enthalpy (J)
I	Current (A)
k	Thermal conductivity (W/mK)
λ	Specific latent heat (J/kg)
OCV	Open circuit voltage (V)
ρ	Density (kg/m^3)
Q	Heat transfer rate (W)
\dot{Q}	Volumetric Heat generation rate (W/m^3)
T	Temperature ($^{\circ}C$)
T_{Max}	Maximum temperature ($^{\circ}C$)
T_{Bat}	Battery temperature ($^{\circ}C$)
t_c	Time constant ($^{\circ}C$)
V	Voltage (V)
Vol_{Bat}	Battery volume (m^3)
v_a	Ambient velocity (m/s)

1. Introduction

The main power source of electric vehicles (EVs) comes from the lithium-ion battery pack installed across the undercarriage of the vehicle. Lithium-ion batteries and their variants are the preferred energy source for EVs due to their high power-to-weight ratio, energy density and specific energy. These batteries operate optimally under specific temperature conditions and exposure towards extreme temperature conditions would lead to accelerated degradation of the battery pack. Hence, EV manufacturers make it a priority to regulate the temperature of these packs through Battery Thermal Management (BTM) systems.

1.1 Market Demand for EVs

With the rise in global energy consumption, the need for renewable energy sources is increasing, particularly in the transportation sector which accounts for 26.6% of global energy consumption in 2012 (Valavanidis, 2018). From this total, passenger or personal mobility-related fuel consumption accounted for 61% of total world transportation energy consumption (U.S. Energy Information Administration, 2016). Thus, there is a strategic need to increase the usage of renewable energy sources in personal transportation vehicles in order to ensure the sustainability of energy delivery into the future.

Traditional internal combustion engine vehicles (ICEVs) may not be sustainable for future usage due to the ongoing depletion of petroleum as a non-renewable natural resource. As such, EVs are attractive alternatives for long-term usage as electricity can be extracted from renewable energy sources such as wind/solar farms. There is also steady growth in battery recycling techniques and great improvements in battery capacities allowing for greater mileage (Gaines, 2018; Nishi, 2014). Furthermore, ICEVs have an efficiency rating of 20~30% whereas EVs have efficiency ratings greater than 90% (Marques et al., 2011).

Presently, EVs are gaining popularity in global markets. According to the Global EV Outlook 2020, there has been exponential growth in the deployment of electric vehicles with approximately 7 million EVs owned in 2019 as graphed in Fig. 1 (International Energy Agency, 2020). Though figures for 2020 EV sales are projected to be lower due to the novel coronavirus pandemic that began in December 2019, historical data indicates that there is much greater long-term potential (Bloomberg, 2020).

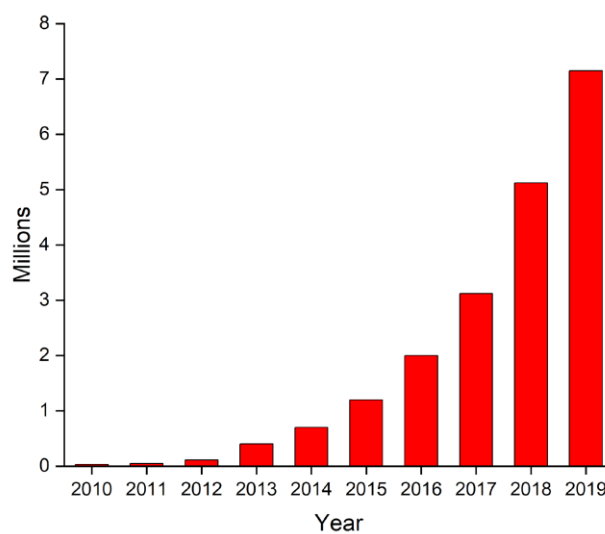


Fig. 1 Deployment of electric vehicles over the past decade (International Energy Agency, 2020)

While the demand for EVs is expected to continue rising as the technology matures, there exist significant barriers towards more widespread adoption of EVs, which are primarily their high upfront costs and limited battery longevity. Typically, a domestic wall charger for an EV would cost around €1,049. Though in certain countries such as Ireland, Japan and the Philippines, government incentives can reduce its cost down to €449.00 (May, 2018). As for the cost of the EV itself, a great proportion of its price stems from its batteries. Based on studies conducted by Kochhan et. al., it is estimated that EV battery packs - typically lithium-ion batteries due to

their high energy density - constitute 35-50 % of the total cost of an EV as displayed in Fig. 2 (Kochhan et al., 2014).

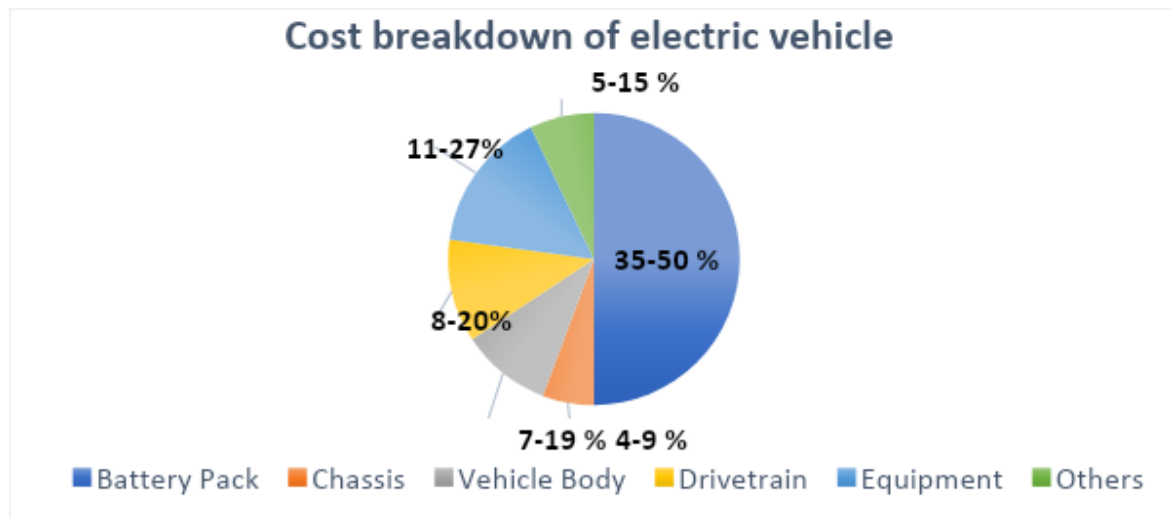


Fig. 2 Cost breakdown of an electric vehicle (Kochhan et al., 2014)

One way to reduce the overall cost of EVs is to improve battery longevity or efficiency. Currently, EV battery packs are warranted towards an average range of 160,000 km (Battery University Group, 2020). Extending the lifespan of the battery would reduce the frequency in which the battery would have to be replaced which in turn would reduce the long-term cost of owning an EV. There are several parameters that could be improved and optimized across a battery pack ranging from its electrochemistry to its geometry. EV Battery performance, properties, reactions, efficiency, and safety are also further susceptible towards ambient conditions, notably temperature. Thus, good BTM is needed to assist in regulating these conditions to ensure optimal performance of the battery.

1.2 Significance of Battery Thermal Management (BTM) System

BTM systems are important to maintain EV battery packs within an ideal operating temperature range in order to extend battery longevity. The permissible operating temperature of lithium ion (Li-ion) batteries is between -20 – 60 °C but they are ideally operated between 15 – 35 °C. Deviances outside the optimal temperature ranges would degrade battery performance, depending on whether the battery is above or below the ideal range as highlighted in Fig. 3 (Pesaran et al., 2013).

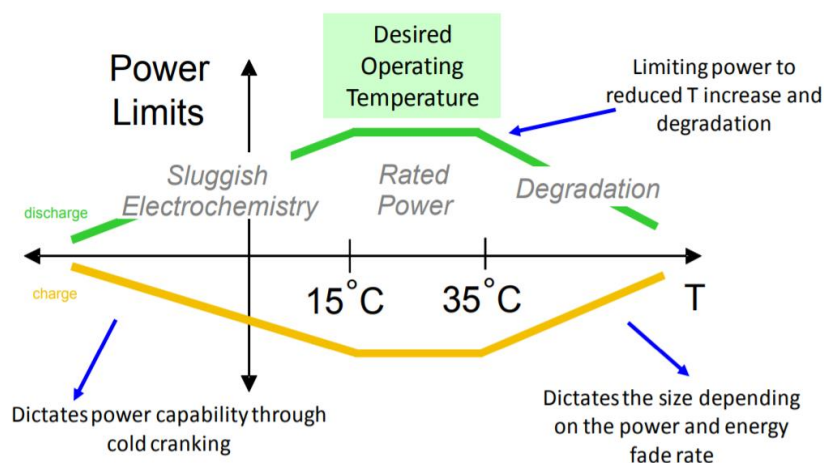


Fig. 3 Ideal operating temperature of a lithium-ion battery (Pesaran et al., 2013)

The battery's internal temperature is influenced by 2 major factors, which include its charge/discharge rate and ambient temperatures. As the charge rate (C-rate) of the Li-ion battery increases, so does the rate of temperature rise across the battery. C-rates are measured based on the time needed to charge a battery until it is fully charged. A 0.5C charging rate Li-ion battery would take 2 hours to reach a 100% state of charge (SOC) while a 1C battery would take an hour and a 2.0C battery would take 30 minutes. Most Li-ion batteries are rated to be charged between 0.5C and 1.0C to minimize the risk of thermal degradation across the battery. However, recent V3 supercharging stations supplied by Tesla Inc. have managed to advance

charging stations to as high as 1.5C, requiring only 2400 seconds to reach 100% SOC, as displayed in Fig. 4 (Lambert, 2019).

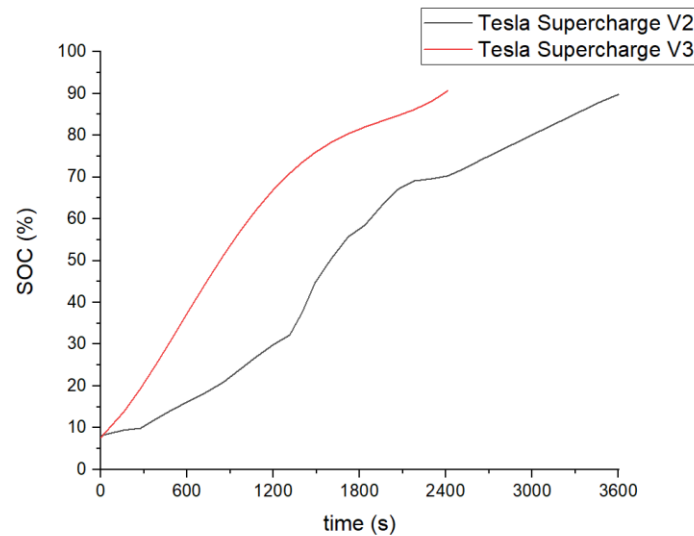


Fig. 4 Tesla's latest supercharging station charges at a 1.5C rate (Lambert, 2019)

Further improvements in C rates for future charging stations would necessitate advancements in battery cooling technologies to mitigate the amount of heat released during accelerated charge rates.

While charge rates do cause thermal energy to be generated from the batteries core, ambient heat transfers thermal energy to the battery through radiative heat. The permitted charging temperature range of Li-ion batteries are narrower than the battery's permitted operating temperature, with charging temperatures being between 0 ~ 45 °C (Battery University Group, 2017).

1.2.1 Low Temperature Effects

Cold temperatures affect Li-ion batteries both physically and chemically. Physically, cold temperatures decrease the viscosity of the electrolyte, causing a reduction in ionic reaction rates while polymerous portions of the battery would also become brittle (Ma et al., 2018).

Additionally, low temperatures accelerate the growth of dendrites within the battery, which would compromise the safety of the battery and reduce the battery life. Chemically, the internal resistance of the battery would become lower, which would in turn lower the relative capacity of the battery as the temperature drops. While the battery's relative capacity would degrade naturally over a combination of prolonged charge/discharge cycles and calendar aging, it is accelerated when exposed to the cold (Chang, 2019). The effect is most pronounced when the battery's temperature is below $-10\text{ }^{\circ}\text{C}$ as shown in Fig. 5.

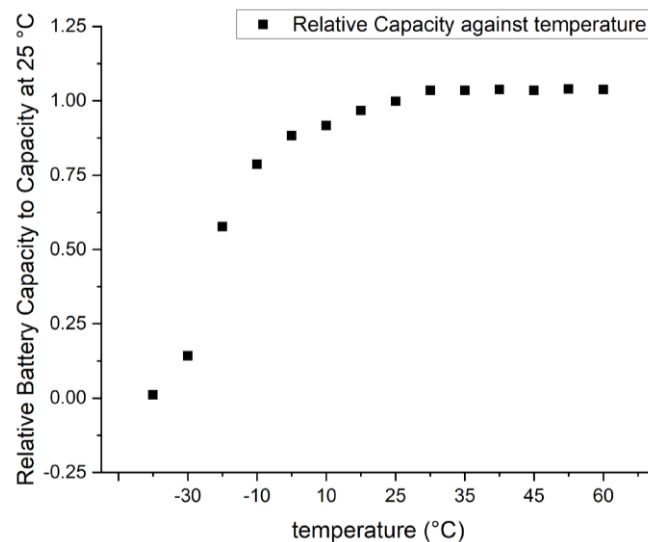


Fig. 5 Change in relative battery capacity as the Li-ion battery's temperature changes (Chang, 2019)

Manufacturers account for capacity degradation through prolonged use by allocating additional capacity to ensure that the EV is able to perform at the rated capacity throughout its vehicular lifespan as shown in Fig. 6 (Battery University Group, 2018). However, the additional capacity may not be sufficient to offset low temperature degradation if temperatures are too low. Thus, the incorporation of BTM systems is crucial for prolonged usage of an EV.

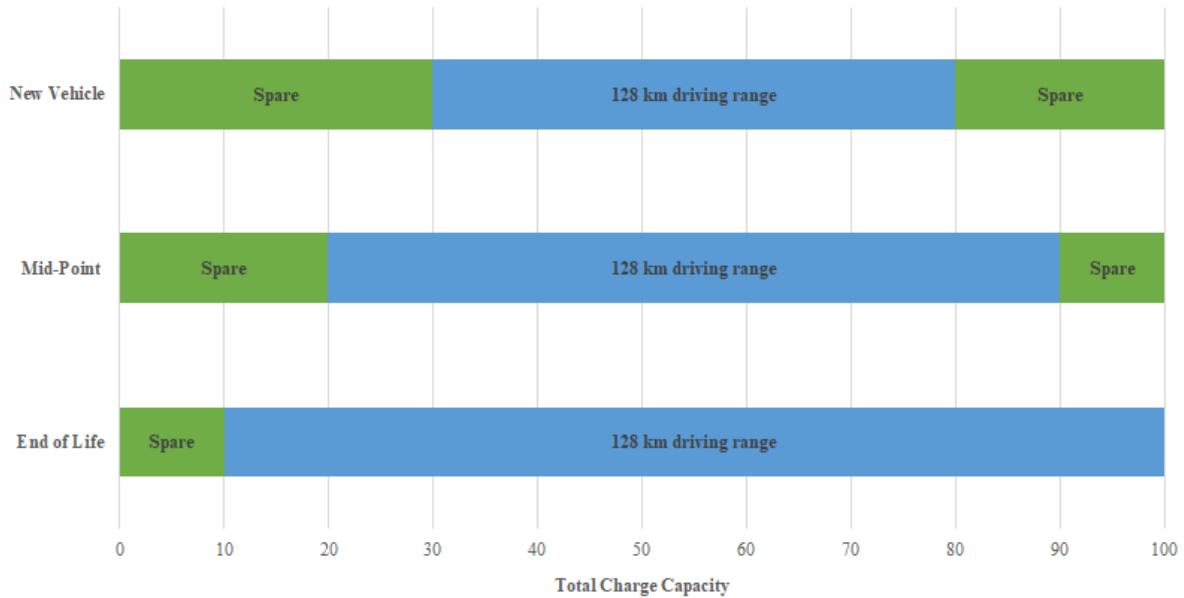


Fig. 6 Vehicle driving range relative to battery life (Battery University Group, 2018)

1.2.2 High Temperature Effects

There are 2 primary concerns when Li-ion batteries go above the optimal range of 15–35 °C, which are accelerated aging across the battery and the risk of thermal runaway. Similar to the effects of cold temperature exposure, Li-ion batteries age quicker when exposed to high temperatures as the cathode structure of the battery becomes compromised (Ma et al., 2018). In regards to thermal runaway (TR), there is a high risk for the Li-ion battery to undergo TR when subjected to thermal abuse (Feng et al., 2017). The risk of a chain reaction leading to TR gets exponentially higher as the battery’s temperature goes above 60°C as displayed in Fig. 7 below (Feng et al., 2017). Typically, manufacturers would introduce various safety mechanisms to prevent this from occurring. The installation of a BTM system is an example of one of those systems.

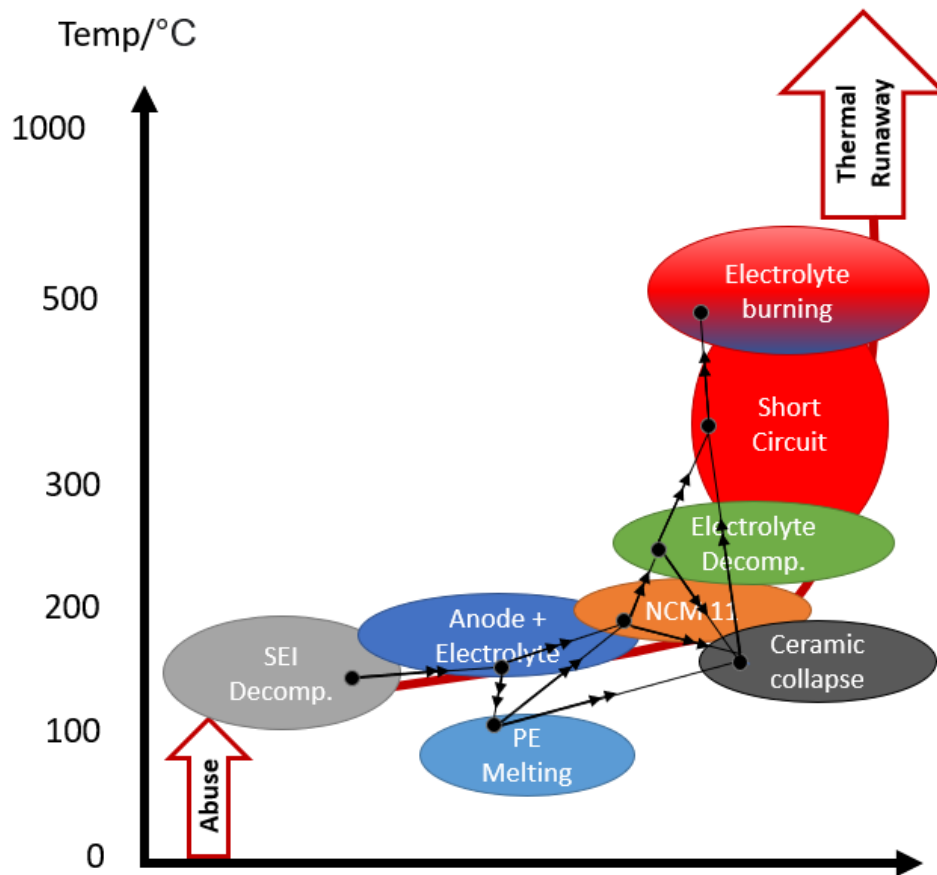


Fig. 7 Chain reaction that leads to thermal runaway (Feng et al., 2017)

1.3 Project Scope and Vision

At present there are several existing BTM systems available in the current EV market, which typically consist of air-based, liquid-cooled and refrigerant-based cooling systems. Each system has its respective advantages and disadvantages, which will be further covered in the Literature Review. Nevertheless, each of these systems share a common disadvantage - they require an active component such as a pump or a fan. Such components require additional spacing within the EV and require additional power to operate, resulting in lower efficiencies across the EV.

Phase change material (PCM) based BTM systems could potentially be utilized as alternatives to conventional air, liquid and coolant-based cooling systems due to PCMs having high latent heat storage capacities. There are multiple PCM types with differing thermophysical properties used in varying industries including solar, construction and manufacturing. As such, the cooling requirements of the application should first be considered before determining the PCM type to be used. With regards to Li-ion BTM, paraffin bolsters several suitable qualities including excellent thermal and chemical stability, non-corrosivity, high latent heat capacities, and low costs (Himran et al., 1994). Despite such beneficial traits, there are two major considerations that should be addressed when utilizing PCMs, including enhancing their thermal conductivity, as PCMs are generally poor heat conductors, as well as designing the method of containment (Advanced Cooling Technologies, 2019; Alam et al., 2015). The container used has to fulfil several requirements including preventing PCM spillage during the melting process, maintaining sufficient heat transfer between the heat source and the PCM, and providing sufficient void space to accommodate for PCM expansion during the melting process (Advanced Cooling Technologies, 2019). As such, the study conducted aims to fulfil the following objectives:

- (1) Designing a prototype that can house a standard 18650 battery while simultaneously regulating its temperature.
- (2) Determining the heat transfer rate, \dot{Q} of a typical 18650 cell under varying discharge rates.
- (3) Identifying the optimal PCM type to be used for Li-ion battery temperature regulation.
- (4) Optimizing the prototype to effectively transfer heat away from the battery to the PCM with as little volume possible.
- (5) Simulate the effectiveness of the prototype under various ambient temperatures.

2. Literature Review

2.1 Current BTM Systems

As mentioned in the introduction, a BTM system is paramount for the safe and optimal operation of Li-ion battery packs. This has helped spur innovation in air, liquid and refrigerant-based cooling systems (Wiebelt and Heckenberger, 2010). Industry engineers typically select one of the three cooling systems based on the space and cooling requirements of the battery pack. This section analyses the advantages and disadvantages of the three BTM systems in comparison to the passive PCM based system.

2.1.1 Air-Based

Air-based cooling systems are typically rudimentary in design but are lighter in weight and easier to service compared to the other cooling systems. Their simplicity stems from the fact that there is no need for insulation between the air and the battery. There is also no risk of spillage, unlike liquid and coolant-based systems. This allows for easier maintenance and more adaptive designs to be utilized across the battery. Such systems utilize ambient air as a cooling medium to regulate the battery's overall temperature. Appropriate mass flow rates should thus be calculated based on the temperature difference between the battery's internal temperature and ambient temperature, as well as the air flow rate and number of batteries used, as described by the formula reported by Xinran et. al. (2014) in Eq. 1.

$$\dot{m}_{air} = \frac{n_{batt}Q_{air}}{c_{p,air}(T_{outlet} - T_{inlet})} \quad (1)$$

In the formula, \dot{m}_{air} is the mass flow rate of air (kg/s), n_{batt} is the number of batteries in the module, Q_{air} is the volume flow rate of air used (m^3/s), $c_{p,air}$ is the air specific heat capacity (J/kgK), T_{outlet} is the outlet air temperature and T_{inlet} is the inlet air temperature.

One example of EVs that use advanced air-based cooling systems in their batteries is the one designed by Siemens that redirects cooled air from the vehicles A/C unit to the battery pack (SIEMENS, 2019).

A major weakness of air-based systems is the lower specific heat capacity of air compared to water and other coolants in a liquid medium. This in turn requires air based BTM designs to accommodate large manifolds, ducts and fans, which would increase the overall size of the battery pack. The whirring of the fans also contributes to the noise pollution of the vehicle. While noise pollution from fans can be easily mitigated using methods such as layer damping, ductwork padding with foam/fiberglass and the installation of vibration isolators underneath the fan, these nevertheless incur additional cost.

Several studies have been conducted on ways to better optimize the manifolds, ducts and fans in air-based cooling systems to overcome existing restrictions and convect more heat from the batteries. Zhang et. al. (2014) utilized a pin fin heat sink design between prismatic batteries to increase the battery's overall heat transfer area. Results from their research indicate that increasing the length of the pins parallel to the direction of the air flow would enhance the temperature uniformity of the battery pack. Chen et. al. (2017) proposed a similar pin-finned channel design yielding similar results. Fan et. al. (2019) investigated the effects of changing the arrangements of cylindrical Li-ion batteries within the pack to determine if the maximum temperature rise of the battery would differ. Battery arrangements across the pack included being aligned, staggered and crossed. However, from the results gathered, the arrangements of the battery did not significantly vary the battery's maximum temperature rise.

In a follow up study, Fan et. al. (2019) also studied the effect of increasing the inlet air velocity on the battery's maximum temperature rise. Their results showed that there was a large

decrease in the battery's maximum temperature rise as the inlet velocity increased, even across various discharge rates, as highlighted in Fig. 8 (Fan et al., 2019).

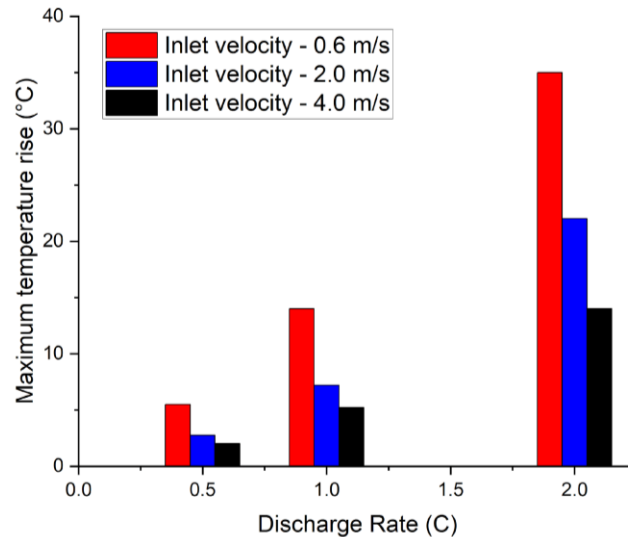


Fig. 8 Maximum temperature rise of Li-ion batteries with respect to increasing inlet air velocities at various discharge rates (Fan et al., 2019)

2.1.2 Liquid-Based

A major advantage of liquid-based cooling systems over air-based systems is the more compact nature of the structure. The higher conductivity, density and specific heat capacity of fluids enable liquid cooling systems to be approximately 3,500 times more efficient than their air-cooled counterpart (Moghaddam and Mazyar, 2018). However, they also come with other disadvantages including higher costs, risk of leakages and greater intricacies in operation (Xia et al., 2017). Liquid systems are greatly affected by varying factors such as the mass flow rate of the liquid, initial inlet temperature of the battery cooling liquid, ambient temperatures, thermal properties of the liquid and geometry of the system. There are two types of liquid cooling systems - indirect liquid cooling and immersion cooling.

2.1.2.1 Indirect Liquid Cooling

Generally, water is the most commonly used coolant in liquid cooling systems. There are other coolant types such as glycol-water solutions, dielectric fluids, and oils, but the specific heat capacity of water remains the highest (Quesnel, 2017). However, one issue with utilizing liquid cooling systems is the risk of leakage, which could in turn lead to a short circuit. The hazard of electrical conduction can be remedied using the indirect cooling method, which involves wrapping the battery cell with tubing in which the liquid cooling medium may flow through while sustaining high thermal conductivities. This concept is illustrated in Fig. 9 where the cool fluid medium conducts heat away from the battery and flows out through the outflow.

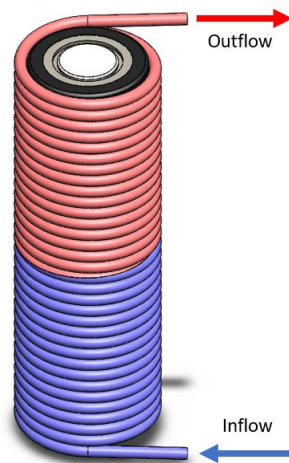


Fig. 9 Liquid medium flows through the tubing while conducting heat away from the battery

One study has also investigated the integration of a cooling plate to conduct heat away from the battery (Panchal et al., 2015). Such systems reduce the risk of a short circuit, as the cooling plate acts as a barrier between the battery and the liquid medium. Prismatic and pouch cell designs are particularly suited to the use of such cooling plates, as they have wider surface areas that allow greater heat transfer through the cooling plate. However, cylindrical batteries such as those of a typical 18650 cell do not benefit as much from cooling plates due to the absence of a flattened surface area. As such, EV manufacturers such as Tesla generally install

cooling ribbons instead, which are able to conform to the limited spacing across the cylindrical based battery pack, allowing them to transfer heat more efficiently away from the battery as illustrated in Fig. 10 (Bower, 2018).

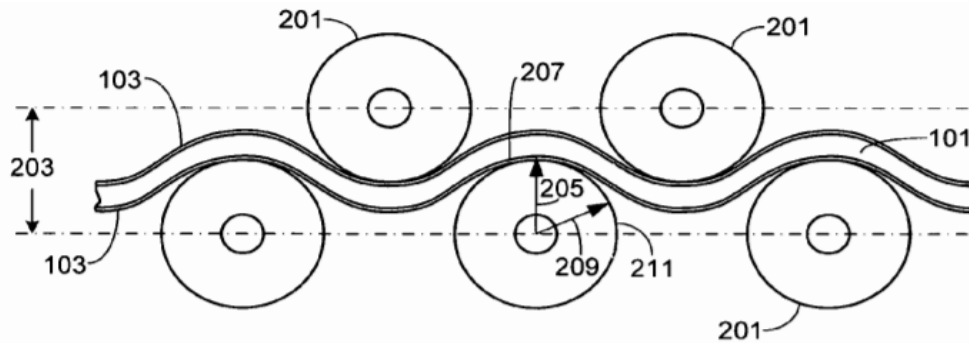


Fig. 10 Ribbon cooling across a Tesla battery pack (Bower, 2018)

In terms of effectiveness, the higher the mass flow rate of the liquid medium, the greater the heat dissipation across the battery. Lai et. al. (2019) demonstrated this correlation through a novel liquid BTM system, with their results indicating that the higher the mass flow rate of liquid going through the inlet, the lower the overall maximum battery temperature rise, as observed in Fig. 11.

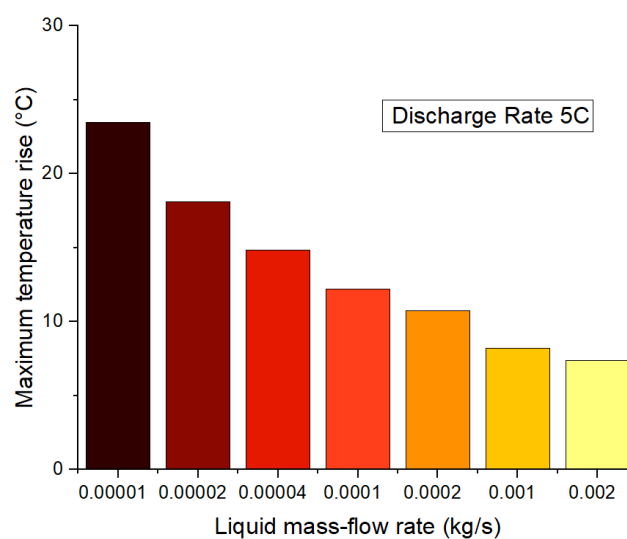


Fig. 11 Maximum temperature rise of a cylindrical 18650 cell discharged at 5C cooled using a novel liquid BTM system (Lai et al., 2019)

2.1.2.2 Immersion Cooling

Immersion cooling involves submerging an electrical component such as a battery pack into a dielectric fluid such as mineral oil or silicon oil to cool it. While dielectric fluids have lower thermal conductivities than water, their insulative properties allow for the complete immersion of an electric circuit, resulting in substantially greater heat transfer potential (Sundin and Sponholtz, 2020). This also allows for greater temperature uniformity across the battery pack. Other properties of dielectric fluids used in immersion cooling include low viscosity, high thermal capacity, and high thermal conductivity.

Currently, this technology is used mostly for power electronics, data centre servers, and racing EVs (Mathur et al., 2014; Wang et al., 2009) Its application in conventional commercial EVs is currently not widely observed due to the high cost of dielectric fluids and the risk of leakage if the container is not properly sealed. Additionally, dielectric fluids such as mineral oils contain sulfuric elements which would corrode the steel container that houses the battery cell, which would in turn accelerate battery failure (Sundin, 2018).

2.1.3 Refrigerant-Based Cooling

An alternative to air and liquid cooling-based systems is to cool the batteries directly through evaporator coils. Essentially, an additional set of evaporator coils is retrofitted parallel to the existing HVAC system meant for cabin climatization within the vehicle to cool the battery pack as illustrated in Fig. 12 (Christian et al., 2017; Pankaj, 2017). This concept allows for a reduction in the number of active components, allowing for a more compact and lighter system (Bauchrowitz et al., 2010). Overall piping can also be reduced due to the utilization of pre-existing pipes for the cabin's HVAC. Heating foils may also be added beneath the battery pack when ambient temperatures are significantly low.

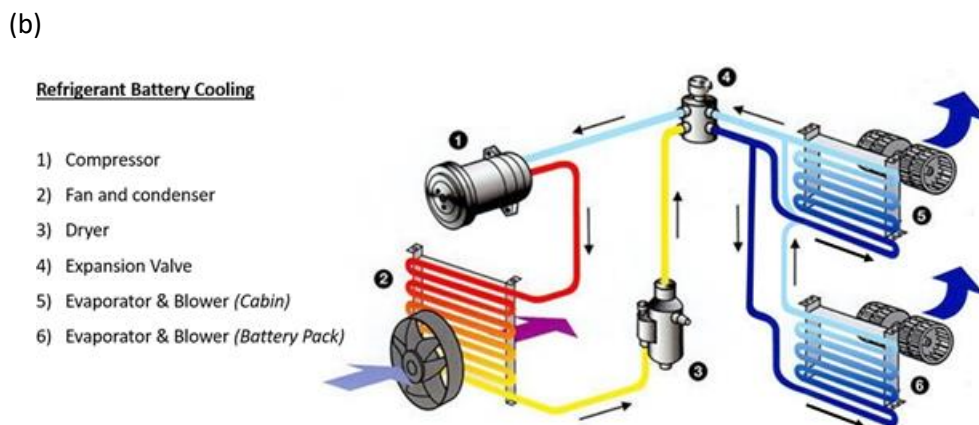
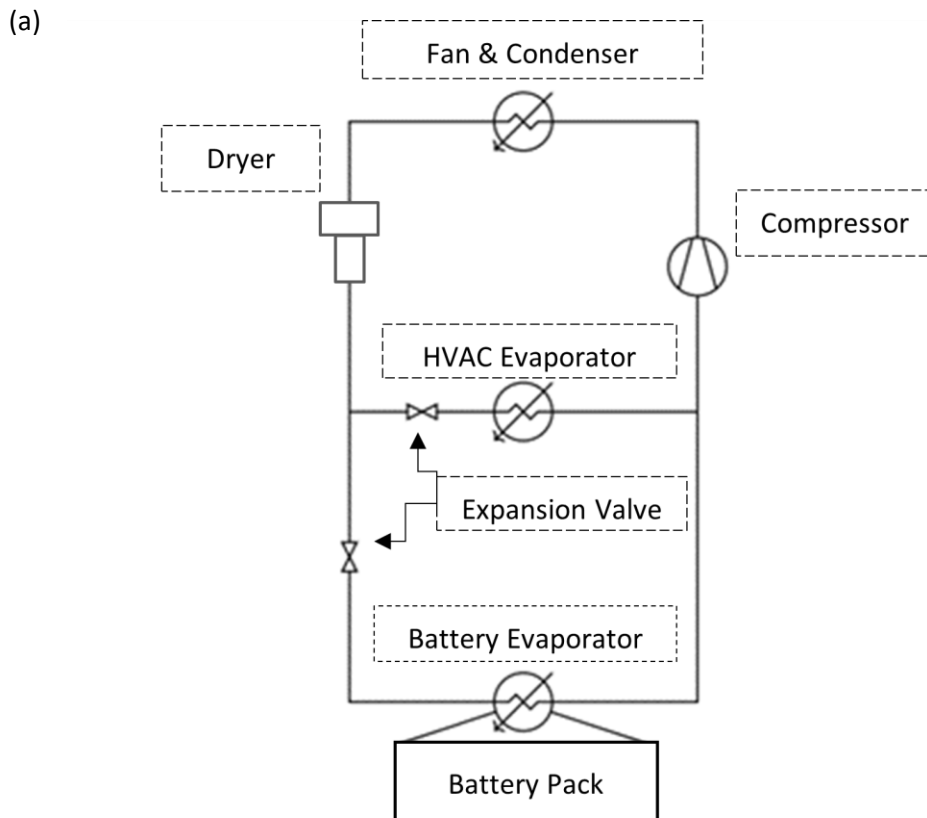


Fig. 12 Refrigerant based cooling system for battery pack cooling (a) Simplified diagram of the refrigerant based cooling system (b) 3D visualisation of the system (Christian et al., 2017)






























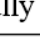




A weakness of this model is that when there is an increase in the battery cooling demand such as during rapid acceleration and high battery charge rates, the fan must use additional energy to cool the condenser coils. While the overall system efficiency can be improved greatly while the vehicle is being driven, its practicality drops while the vehicle's cabin does not require

cooling, but the battery still requires high temperature loads. For instance, while the vehicle is charging, the air conditioning system would have to be switched on to regulate the battery's temperature.

2.1.4 Comparison Between the Various Cooling Systems

Each cooling system has its advantages and disadvantages, making it challenging to identify which system is the best as a BTM system. Christian et. al. (2017) has created a table that summarises the effectiveness of each system based on their corresponding traits as shown in Table 1.

Table. 1 Comparison of the effectiveness of varying cooling system types (Christian et al., 2017)

Criteria	Cooling System		
	Air Cooled	Liquid Cooled	Refrigerant
Cooling efficiency			
System complexity			
Ease of use			
System weight			
System volume			
Cooling power			
Cooling uniformity			
Heating integration			
Initial system cost			
Maintenance effort			
Requirements:  Not met  Partly met  Mostly met  Fully met			

Air cooled systems are lighter, cheaper and simplistic in design but have low cooling efficiencies. Liquid cooled systems have higher cooling efficiencies and are compact but require more weight, cost and design complexity. Refrigerated systems have the highest

cooling efficiency and compactness with moderate weight load, but they also have the highest cost.

2.2 PCM Thermal Management

Conventional EV BTM systems using air, liquid or refrigerant based cooling systems require additional energy to cool their battery packs. This in turn leads to lower mileage efficiencies across the vehicle as energy is also diverted to the BTM system itself. A potential alternative substitute to such BTM systems is phase change material (PCM) based BTM systems. PCMs contain high latent capacity which in turn allows them to dissipate the conducted heat and regulate temperature passively. Additionally, PCMs can alternate between storing and releasing thermal energy during the battery recharge cycle. Thermally, the PCM first absorbs heat as sensible heat, and as it approaches the transition point, it begins to absorb heat as latent heat. As the PCM cools down, it solidifies and releases its stored energy back to its ambient surroundings (Berthou, 2011). Fig. 13 displays the phase change cycle as PCM temperature rises and falls.

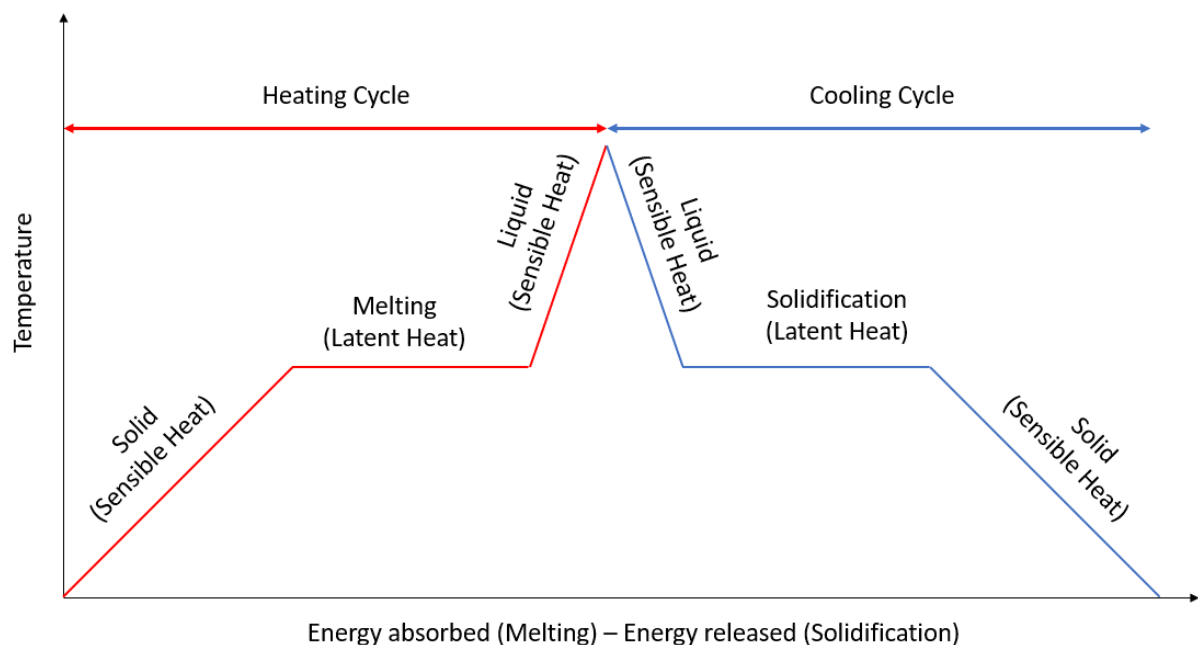


Fig. 13 The phase change cycle of the PCM in relation to the change in temperature of the PCM

As solids have lower specific heat capacities than liquids, the main utility of PCMs come from their phase change and liquid state, when more latent and sensible heat can be absorbed with minimal rise in the temperature of the PCM (Ed et al., 2020). As such, the melting point of the PCM selected should be close to the maximum temperature requirement of the application used to ensure the greatest amount of heat can be transferred. Extensive research has been conducted on the utilisation of PCMs in EV BTM systems, as well as in other applications including building climate control and solar hot water storage systems (Lauf and Hamby, 1990). There are numerous PCM types with various thermo-physical properties, most notably in terms of melting temperatures and latent heat capacities. PCMs can be mainly divided into two main groups - inorganic PCMs and organic PCMs (Sharma et al., 2009).

2.2.1 Inorganic PCMs

Inorganic PCMs used for latent heat storage are typically metals, salts and salt hydrates. These PCM types are non-flammable and have high latent heat energy, good thermal conductivity as well as low thermal expansions. These properties allow them to absorb large quantities of heat while occupying a smaller volume compared to organic PCMs. However, the melting temperature of inorganic PCMs are between the 307 ~ 380°C and 700 ~ 900°C range, while the melting temperature of organic PCMs are at the 5 ~ 380°C range (Biswas, 2016). These high phase change temperatures make inorganic PCMs unsuitable for most consumer applications. Inorganic PCMs are also corrosive, and their melting points tend to change when used for prolonged periods (Ianniciello et al., 2018). Therefore, inorganic PCMs like salts are mostly used for high thermal energy storage applications at the industrial level such as solar power plants but rarely applied in consumer BTM applications. (Mathur et al., 2014).

2.2.2 Organic PCMs

Organic PCMs are carbon and hydrogen-based compounds. One example of a common organic PCM is paraffin, with a chemical formula of C_nH_{2n+2} . As the length of the hydrocarbon chain increases, so too does its melting temperature and latent capacity (Wang et al., 2009). Other organic PCMs include fatty acids, esters, alcohols, and glycols. The melting temperatures of these substances range from 15–130 °C and their melting point does not change significantly even after prolonged periods of use. Chemically, these substances are stable, non-corrosive and have high latent heat.

However, they have two major weaknesses, which are their high flammability and poor thermal conductivity, resulting in sluggish heat transfer rates and high temperature gradients during the charging and discharging process (Farid et al., 2004). These flaws can be overcome using several thermal conductivity enhancement techniques including the addition of metallic fins or extended surfaces, incorporation of metal-based additives and installation of heat pipes (Joybari et al., 2017; Mantilla Gilart et al., 2012). Thermal conductivity enhancement will be further elaborated on in Section 2.2.4.

2.2.3 Comparison of Inorganic and Organic PCMs

An overview of several PCM types is displayed in Fig. 14. While inorganic PCMs such as carbonates and chlorides have both wider melting temperature ranges and higher latent heat energies, organic PCMs such as paraffin and fatty acids have melting temperature ranges of around 0~200 °C, which encompasses that of ambient temperatures. This allows organic PCMs to be more suited towards BTM applications which generally run between 15~35 °C. Briefly, while salt hydrates and gas hydrates also have melting temperature ranges close to ambient temperatures, it was decided not to use them for BTM applications due to the risk of corrosion.

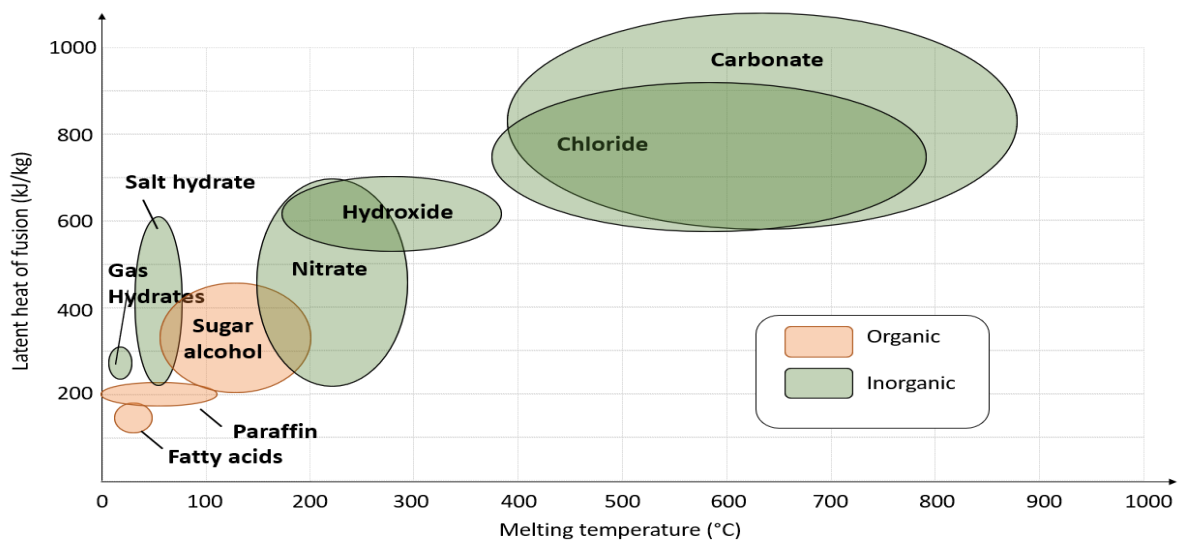


Fig. 14 Overview of PCM types based on melting temperatures and latent heat capacity (Mehling and Cabeza, 2008)

Thermophysical data on various PCM types are difficult to obtain due to the novelty of PCM usage. In Table 2, these values are compiled from several sources from literature. Observably the melting temperatures of inorganic PCMs are much higher than that of organic PCMs. For BTM systems, such melting temperatures would not be suitable for the optimal temperature range of batteries are between 15~35 °C. Latent heat capacities of both the organic and inorganic PCMs vary in range from 75 kJ/kg to 335 kJ/kg. Ideally, the PCM selected for the

BTM system should contain a high latent heat capacity to absorb as much heat as possible from the battery. However, the selection of the PCM for the BTM system is still constrained to the melting point that is within the optimal temperature range of the Li-ion battery to ensure that the batteries' temperature is well regulated in the 15~35 °C range.

Table 2 Thermophysical properties of varying PCM types (Agyenim et al., 2010; Durakovic and Torlak, 2016; Fukai et al., 2003; Medved' et. al., 2016; Pincemin et al., 2008; Zivkovic and Fujii, 2001, Sundararajan et al., 2017)

Compound	Melting temp, T_{melt} (°C)	Latent heat capacity, λ (kJ/kg)	Specific heat capacity, C_p (kJ/kgK)		Thermal conductivity, k (W/mK)		Density, ρ (kg/m ³)		Ref.
			Liquid	Solid	Liquid	Solid	Liquid	Solid	
H_2O (Organic)	0	335.0	4.2	4.2	2.4	0.6	997	920	Agyenim et. al.
Rubitherm, RT 27 (Organic)	27	122.8	4.6	2.3	0.2	0.2	880	760	Durakovic et. al.
Paraffin Wax (Organic)	32-32.1	251.0	3.3	1.9	0.2	0.5	830	-	Zivkovic and Fujii
PEG 900 (Organic)	34	150.5	2.3	2.3	0.2	0.2	1100	1200	Sundararajan et. al.
Medicinal Paraffin (Organic)	40-44	146.0	2.3	2.2	2.1	0.5	830	-	Medved et. al.
Lauric Acid (Inorganic)	41-43	211.6	2.3	1.8	1.6	1.6	1760	862	Medved et. al.
$ZnCl_2$ (Inorganic)	280	75.0	0.7	-	0.5	0.5	-	2907	Pincemin et. al.
$NaNO_3$ (Inorganic)	310	172.0	1.8	-	0.5	0.5	-	2260	Pincemin et. al.
NaOH (Inorganic)	318	165.0	2.1	-	0.9	0.9	-	2100	Pincemin et. al.
KNO_3 (Inorganic)	330	266.0	1.2	-	0.5	0.5	-	2100	Pincemin et. al.

2.2.4 PCM Encapsulation and Thermal Conductivity Enhancement

Thermal conductivity enhancement plays a vital role in the commercialization and viability of PCM-based BTM systems. Several studies have been conducted on these enhancements such as the addition of thermal conductivity enhancers like carbon and metallic nanoparticles, the introduction of metallic fins/tubing to increase the heat transfer area and through micro and macro encapsulation of the PCM (Chen et al., 2017; Fan et al., 2019; SIEMENS, 2019; Wiebelt and Heckenberger, 2010; Zhang et al., 2014).

The inclusion of carbon and metallic nanoparticles to enhance thermal conductivity has been investigated by several researchers. Lin et. al. (2018) reported that the addition of carbon nanoparticles is comparatively more effective at increasing thermal conductivity than metallic nanoparticles. Li and Zhai (2017) supported these findings through their studies on solar collector-storage systems. Their systems utilize both a PCM composite consisting of erythritol and expanded graphite together with aluminium piping. Their results showed that a PCM composite with 3 percent of total weight expanded graphite can increase heat storage efficiencies by 40.17%. Similarly, Choi et. al. (2014) reported that adding graphite amounting to 5.0% of the PCM volume improves the thermal conductivity performance by 3.5 times. However, the addition of such nanoparticles would cause the settling or floating of additives across the PCM during its liquid state. This is undesirable as the cooling rate would become uneven around the battery, leading to chemical instability. Adequate and frequent mixing would be required to ensure uniformity across the PCM medium if such additives are mixed inside it.

The integration of fins or tubing across a heat pipe has numerous advantages in the enhancement of PCM thermal conductivity. The length of fins across the tubing structure ensures thermal uniformity throughout the PCM (Agyenim et al., 2010). Thermal conductivity

efficiency of PCMs is also reported to be significantly higher in fin-based structures compared to PCMs only enhanced with metallic or carbon nanoparticles (Agyenim et al., 2010). Singh et. al. (2019) investigated and compared the thermal conductivity effectiveness of various PCM enhancement methods including the addition of carbon powder, aluminium fins and graphite fins. Results from their study showed that the addition of aluminium fins was the most effective at improving PCM thermal conductivity, increasing it by 42 times, while the carbon fins were the next most effective, improving thermal conductivity by 33 times, as shown in Fig. 15. However, the addition of such fins would increase the manufacturing cost of the PCM container and would thus impose an additional design challenge in terms of weight and complexity.

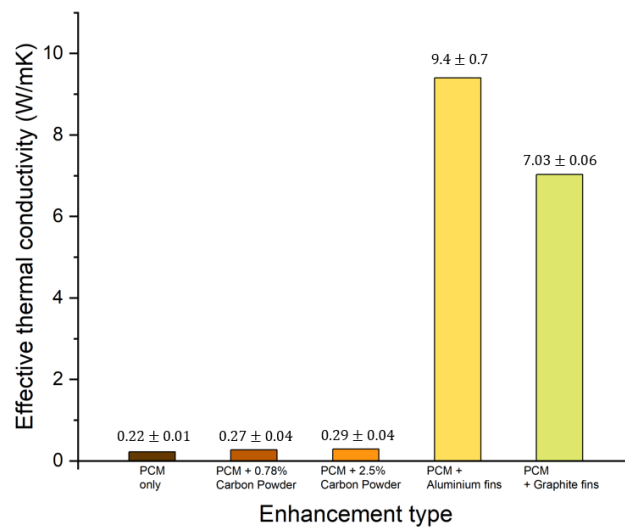


Fig. 15 Effectiveness of various PCM thermal conductivity enhancement types (Singh et al., 2019)

PCM encapsulation involves encapsulating a core material within a shell material. Encapsulation improves heat transfer efficiency by increasing total surface area, prevents environmental contamination of the core material and improves PCM handling (Hassan et al.,

2016). There are generally, two types of encapsulation - microencapsulation, where capsule sizes are between 1–1,000 μm and macro encapsulation where capsule sizes are above 1,000 μm (Salunkhe and Shembekar, 2012). Selection of the core material is based on several factors including application type, thermophysical requirements, acidity and flammability of the material. There are several methods of encapsulating such PCMs including interfacial polymerization, coacervation and phase separation, in-situ polymerization, sol-gel encapsulation, etc (Hassan et al., 2016). However, most of such encapsulation techniques are difficult to achieve and require highly specialized equipment (Hassan et al., 2016).

A comparison of the various thermal conductivity enhancement types is included in Table 3.

Table 3 Comparison between the various thermal conductivity enhancement types (Alam et al., 2015; Hassan et al., 2016; Salunkhe and Shembekar, 2012)

Enhancement Type	Carbon/metal nanoparticles	Metallic fin across container walls	Micro/Macro encapsulation	
Effective thermal conductivity	◐	●	●	
Ease of handling	◐	◑	●	
Ease of preparation /manufacturing	●	◐	◐	
Cost of enhancement	●	◐	◐	
Requirements:	Not met ◐	Partly met ◑	Mostly met ◒	Fully met ●

With such parameters in mind, the cooling prototype constructed in this study focuses on utilizing aluminium fins. The addition of the aluminium fins to the PCM prototype increases its thermal conductivity, is relatively economical in cost and can be adapted to the container’s shapes as compared to enhancing the PCM with carbon/metal nanoparticles or micro/macro encapsulation. The subsequent sections describe the design concept of the proposed PCM BTM prototype and the method of optimizing the structure to best dissipate heat away from the battery.

3. Methodology

To develop and prototype the PCM BTM system for EVs, the design for the system should be first drafted in accordance with several objectives. These objectives include the enhancement of the PCM's thermal conductivity, allocation of adequate storage space for the PCM, prototype compactness as well as other considerations for design manufacturing. The effectiveness of the system is then simulated and optimized through Computational Fluid Dynamics (CFD) software, namely ANSYS. The CFD method comprises modelling three parts.

- (1) Heat released by the battery under varying discharge rates.
- (2) PCM thermophysical properties during the melting phase.
- (3) Heat transfer between the battery to both the PCM and the prototype.

3.1 Design concept

To reduce the size of the BTM system, a honeycomb structure was considered as it can house the battery, contain the PCM, reduce spacing between battery cells and protect the battery pack against physical stress/impact. Utilizing compact geometries across the honeycomb cells would also aid in maximizing the heat transfer between the aluminium structure and the PCM, ensuring sufficient structural strength and reducing the overall volume of the prototype.

Duan et. al. (2019) conducted a study on the melting behaviours of PCMs in honeycomb structures with varying core geometries such as triangular, trapezoid, rectangular and hexagonal, as illustrated in Fig. 16 (a).

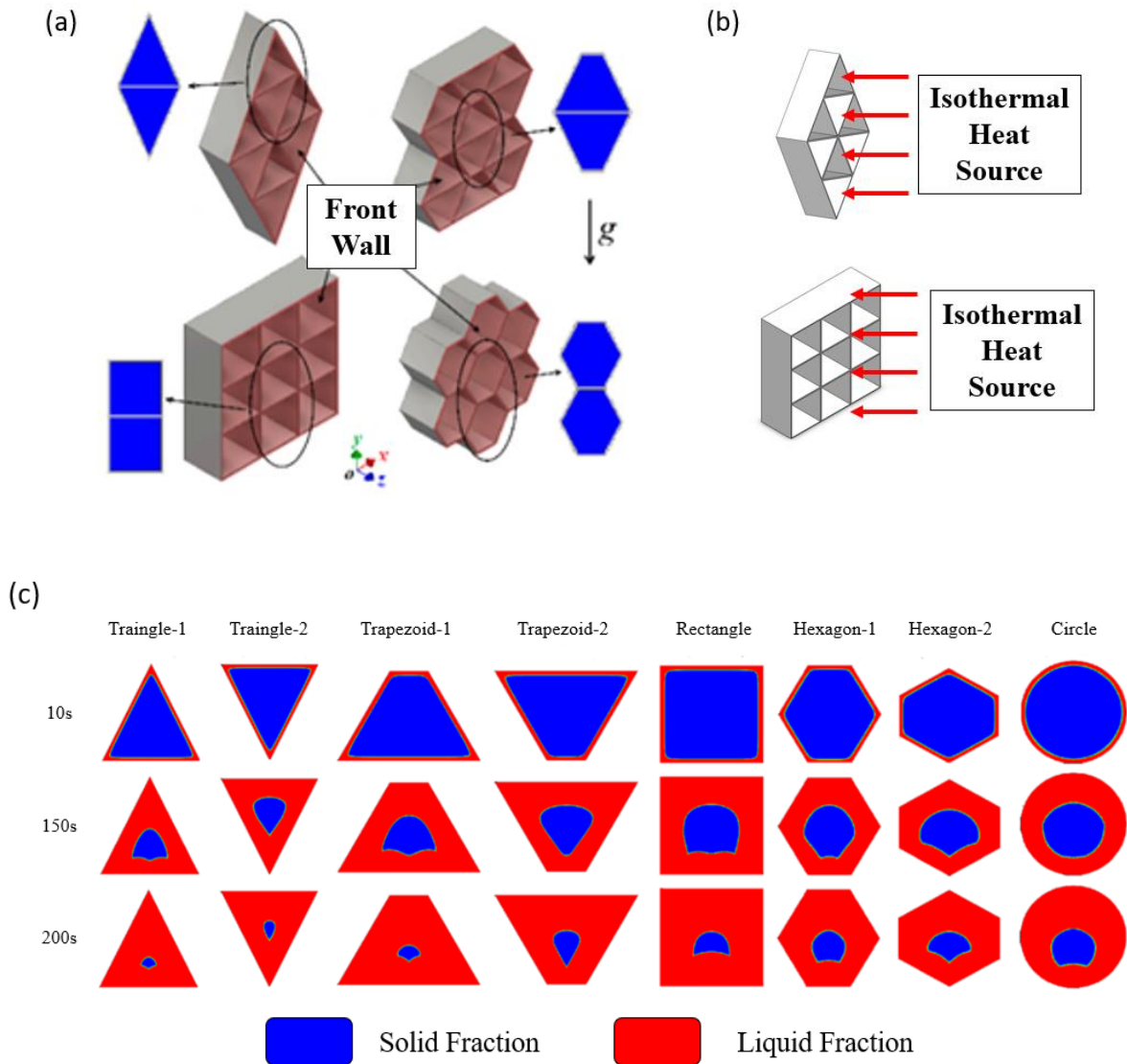


Fig. 16 Effects of various geometries on the rate of heat transfer across PCM in an aluminium container (a) Honeycomb structures were constructed using triangular, trapezoid, rectangular and hexagonal core geometries (b) Isothermal heat source was introduced along the front-wall of the honeycombs (c) Liquid (red) vs solid (blue) fraction of the paraffin within the containers after heating for 10, 150 and 200 seconds (Duan et al., 2019)

In the study, aluminium containers of varying geometries (triangular, trapezoidal, squared, hexagonal and circular shapes) were modelled through CFD to observe how the container

geometries would affect the PCM melting rate when exposed to heat, as illustrated in Fig. 16 (a) and Fig. 16 (b). Additionally, the orientation of the triangular, trapezoidal and hexagonal containers were flipped vertically as shown in Fig. 16 (c) to investigate if orientation affects the heat transfer rate. The isothermal heat source is kept constant across the different geometry shapes. As the solid PCM in the containers were heated for 10, 150 and 200 seconds, the fraction of the PCM that absorbed heat and changed from solid to liquid are illustrated in red in Fig. 16 (c).

Results from the study as shown in Fig. 16 (c) and Fig. 17 indicate that triangular shaped containers have the fastest PCM melting rates, followed by trapezoidal, squared, hexagonal and lastly circular containers. The short time needed for the PCM to completely melt in the triangular containers indicates that they have the greatest heat transfer rate compared to the other geometries.

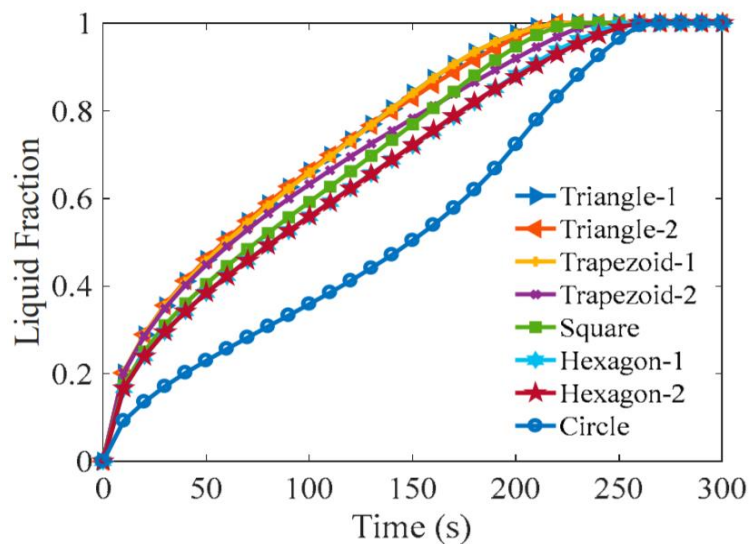


Fig. 17 PCM melting rate based on container geometry type (Duan et al., 2019)

While the thermal performance of a purely triangular honeycomb appears better than other geometries, its structural strength is not comparatively greater. Wang et. al. (2009) compared the structural strength of various metallic honeycomb geometry structures as illustrated in Fig. 18 using a finite element model study.

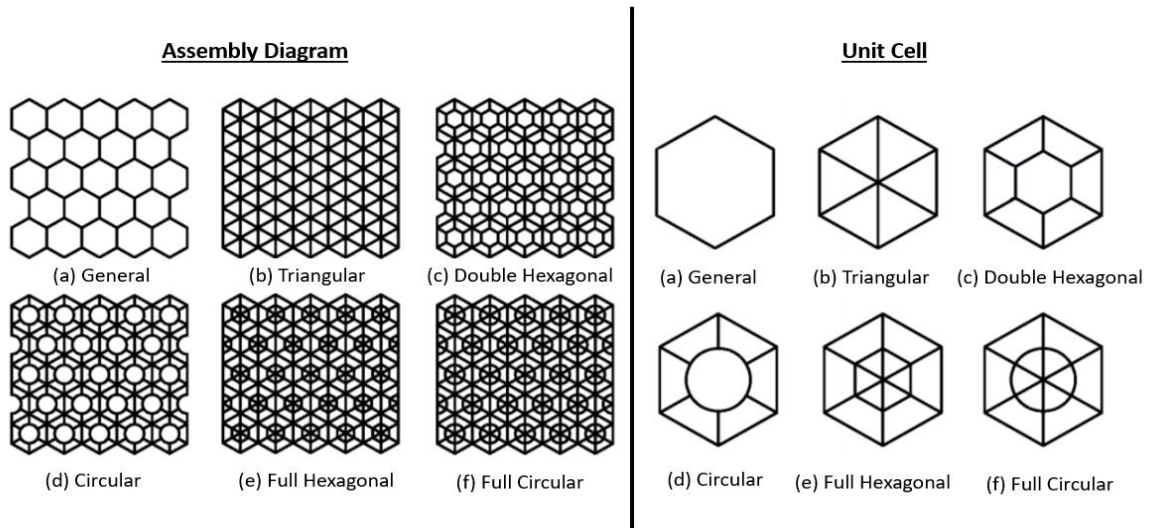


Fig. 18 Varying honeycomb patterns tested for structural strength through finite element model (Wang et al., 2015)

Physical properties of the geometries include a density of 2680.0 kg/m^3 , Young's Modulus of 69.3 GPa , Poisson's ratio of 0.3 and a Yield Stress of 215.0 MPa . Cell sizing of the varying honeycomb structures were set at 1 mm . The varying honeycomb patterns utilized across the investigation were then pressed against a singular contact surface with constant velocity while supported on a static rigid boundary as seen in Fig. 19 below.

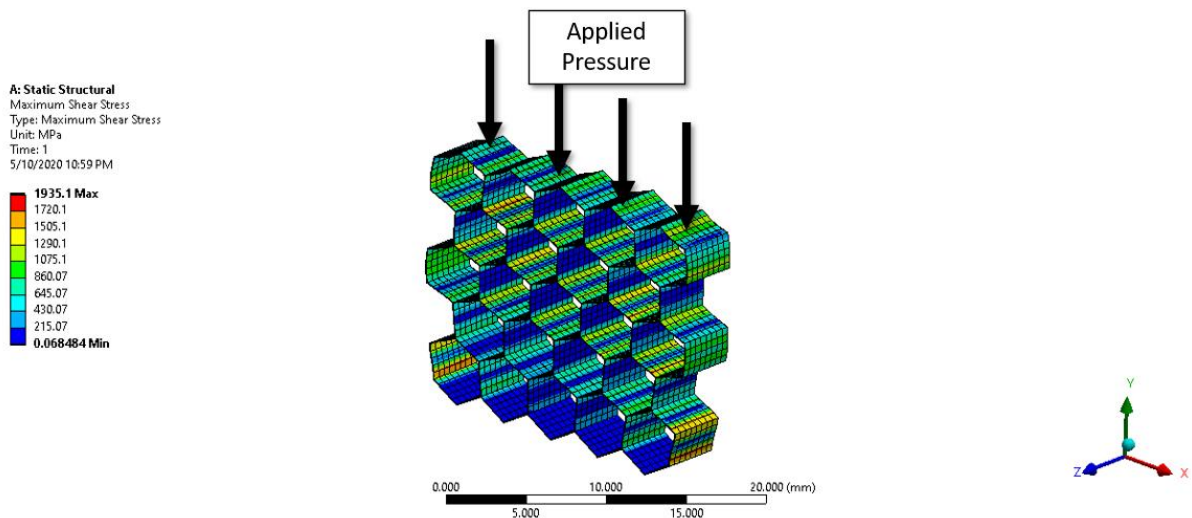


Fig. 19 Example of the general honeycomb body being pressed under a singular contact surface (Wang et al., 2015)

The energy absorbed per unit volume of the various geometries were then tabulated in Fig. 20 below (Wang et al., 2015) to determine the geometry with the greatest strength. Energy absorbed was calculated by obtaining the area underneath the stress strain curve and then dividing it by the geometry's unit volume.

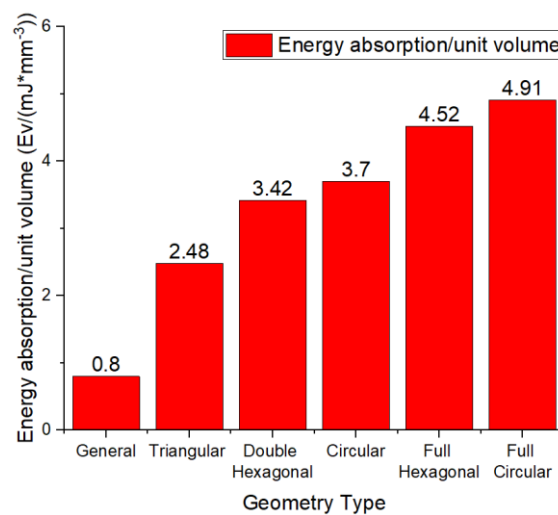


Fig. 20 Structural strength of the varying honeycomb structures measured by the energy absorbed per unit volume (Wang et al., 2015)

It was reported that a honeycomb structure with a central support element as observed in Fig. 18 (c), Fig. 18 (d), Fig. 18 (e) and Fig. 18 (f) are better able to withstand greater stresses and absorb more energy than the other honeycomb design patterns. This is due to the additional support proved by the central column.

With consideration towards both the heat transfer rate and structural strength of each honeycomb geometry and pattern, the design in Fig 18. (d) is proposed for the PCM BTM system design in this project. The reason this design was chosen are as follow:

- (1) It can accommodate a cylindrical battery within its circular core.
- (2) The outer trapezoidal segments would be able to store the PCM and transfer heat from the battery to the PCM efficiently as illustrated in Fig. 16 (c).
- (3) Sufficient structural strength is available across the design due to the circular core within the hexagonal outer shell.
- (4) Does not have any gaps, allowing for maximum space utilization.

The proposed design for the prototype is displayed in Fig. 21 with a diagram of the full assembly on the left and the cell diagram on the right. Further optimization of the structure is explored in Section 5.

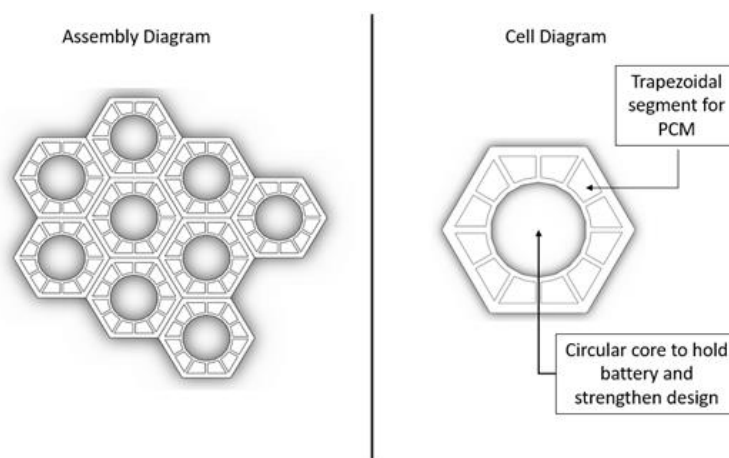


Fig 21 Proposed PCM thermal management honeycomb cell prototype design

3.2 CFD method

With the design of the honeycomb structure established, the PCM thermal management system was further optimized to reduce its overall volume while conducting as much heat away from the battery as possible. There are essentially three parts to the process - identifying the transient heat generation rate from the battery across various discharge rates, modelling the thermophysical properties of the PCM as it absorbs heat during the battery discharge process and finally optimizing the structure of the final prototype with respect to both the transient heat source of the battery and the PCM's thermophysical properties.

3.2.1 Lithium-Ion Heat Generation Model

It is imperative that accurate modelling of the heat generation rate of a Li-ion battery be first established to aid in the optimization of the onboard BTM structure, as well as improve upon the accuracy of the source functions that will be used for future CFD studies. Previous studies (Al Hallaj et al., 1999a; Bernardi et al., 1985; I. Evans and E. White, 1989; Newman and Tiedemann, 1995) have established much of the foundational knowledge of battery heat generation. Most of the works done by the aforementioned research groups acknowledged that the heat generation rate of the battery primarily comprises of both Joule heating and reversible heat generation effects as shown in Eq. (2)

$$Q = I \left[(OCV - V) - T_{Bat} \frac{dOCV}{dT_{Bat}} \right] \quad (2)$$

Whereby Q (W) is the heat generated by the battery, I (A) is the nominal current, OCV (V) is the open circuit voltage, V (V) is the nominal voltage, T_{Bat} ($^{\circ}C$) is the battery's temperature and $\frac{dOCV}{dT_{Bat}}$ is the differential between the open circuit voltage and the battery's temperature. The

first group of values: (i) I ; (ii) OCV ; and (iii) V , represent the irreversible Joule heating effects while the second group: (i) T_{Bat} ; and (ii) $\frac{dOCV}{dT_{Bat}}$, represent the reversible entropic heat produced by the battery. Apart from I , the other variables (OCV , V , T_{Bat} and $\frac{dOCV}{dT_{Bat}}$) in Eq. (2) vary depending on the state of charge (SOC) of the battery. While there are numerous equations that generalize the heat generated by the battery, not many have described a curve-characterization function of the heat generated. Gümüŝsu et al. and Catherino (Catherino, 2015; Gümüŝsu et al., 2017) analysed and plotted the heat generation, Q of a cylindrical and prismatic lithium ion battery respectively at various discharge rates with respect to time, but had not specifically reported the associated heat generation function. The reasoning for this was not explained but it could be assumed that their studies intended for the reader to input their own power profile based on their load type. Nevertheless, the formulation of such a function is conducted to approximate the transient Li-ion battery temperature rise for various discharge rates for this study. Further elaboration of the process and its results are described in Section 4.

3.2.2 PCM thermophysical characteristics and modelling

Similar to establishing the heat generation model of the battery, accurate input of the thermophysical properties of the PCM would be beneficial in approximating the volume of PCM needed for the BTM structure. Throughout a PCM's phase transition process of a PCM, there is a boundary value problem describing the derivative of the PCM's phase boundary with respect to time. This problem is widely known as the Stefan problem. Mathematically the Stefan number, Ste is the ratio between the solid-state specific heat capacity and the latent heat capacity ΔL of a phase changing substance as displayed in Eq. 3.

$$Ste = \frac{c_p \Delta T}{\Delta L} \quad (3)$$

Whereby c_p is the specific heat capacity of the solid PCM, ΔT the change in temperature and ΔL the latent heat capacity. Application of the Stefan problem across a CFD problem assumes that the heat generation source is constant and the melting portion is constantly at the edge of the solid boundary as illustrated in Fig. 22.

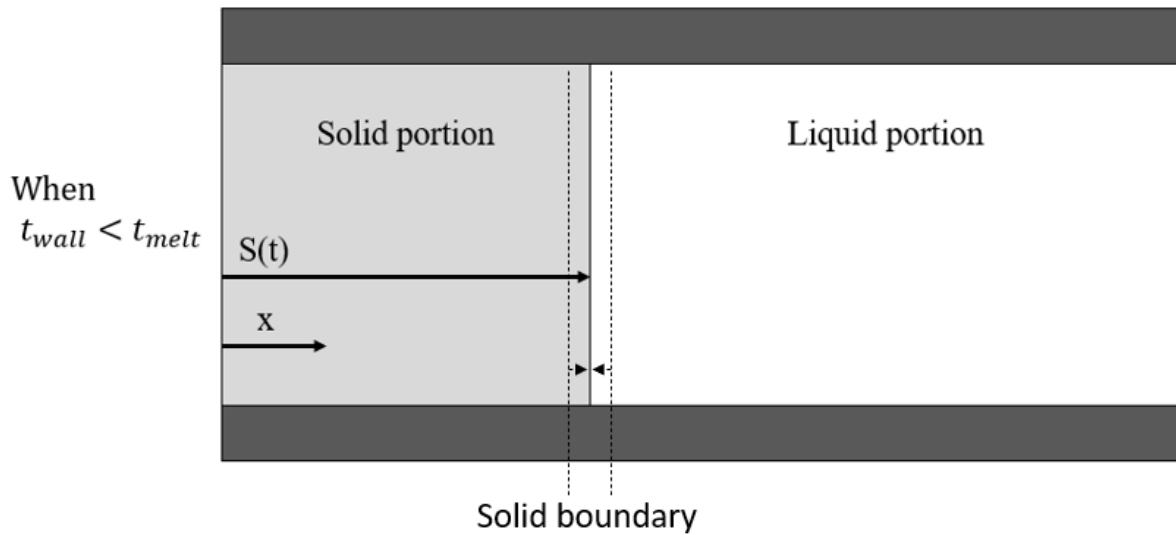


Fig. 22 Representation of the Stefan problem (Sevault et al., 2017)

Whereby t_{wall} is the temperature of the solid boundary, t_{melt} is the melting temperature of the PCM $S(t)$ is the free boundary, x the position in space of the boundary and t the time elapsed (Tobias, 2013). However, the battery's heat generation rate is not constant, as it peaks towards the end of its discharge cycle due to increased Joule heating effects (Gümüŝsu et al., 2017). Thus, it would not be feasible to apply the Stefan problem across the CFD model constructed. To simplify the modelling process of the PCM, the thermophysical properties are assumed to undergo pure conduction with piecewise linear thermophysical properties based on the transient temperature of the battery. The paraffin type used in the study is Rubitherm RT 27, for it has a relatively low melting temperature as compared to other paraffin types (Durakovic and Torlak, 2017). Table 4 displays the thermophysical properties of the RT 27 PCM to be used in the model (Maurizio et al., 2008).

Table 4 Thermophysical properties of RT27 (Maurizio et al., 2008)

Thermophysical properties	Paraffin	Reference
Melting temperatures, T_{melt} (°C)	26-28	Maurizio et. al.
Specific heat capacity (J/kg K)	1800 - 2400	
Specific latent Heat (kJ/kg)	< 200	
Solid density (kg/m ³)	870	
Liquid density (kg/m ³)	750	
Thermal Conductivity (W/mK)	0.09 – 0.05	

It should be noted that the specific heat capacity, c_p peaks during the transitional phase of the PCM. As the melting temperature of the RT27, T_{melt} used is 27.0°C, the c_p value peaks at that range. Fig. 23 displays the transitional specific heat capacity incorporated within the model. A piecewise model was used to approximate the specific heat capacity of the RT27 used.

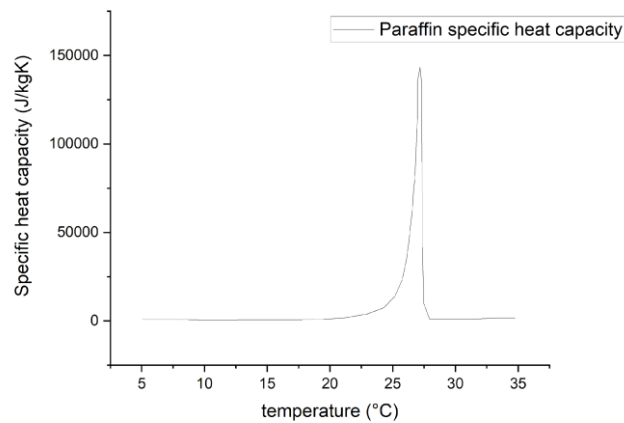


Fig. 23 Piecewise linear model of RT27 specific heat capacity in relation to temperature (Maurizio et al., 2008; Medved' et al., 2016)

The latent heat storage capacity, L , of the PCM can be calculated by integrating the c_p function, $c_p(T)dT$, with respect to the melting range of PCM, T_1 and T_2 . The formula is stated in Eq. 4 (Al-Saadi and Zhai, 2015) below.

$$\int_{T_1}^{T_2} c_p(T)dt = \Delta h_{T_1 \rightarrow T_2} \approx L \quad (4)$$

Whereby c_p ($J/K\ kg$) is the specific heat capacity of PCM, T ($^{\circ}C$) is the PCM's temperature with respect to time, T_1 ($^{\circ}C$) is the temperature at which the PCM starts to melt, T_2 ($^{\circ}C$) is the temperature at which the PCM completely melts, h (J) is the PCM's enthalpy and L (kJ/kg) is the latent heat storage capacity of the PCM.

The thermal conductivity of the PCM drops significantly from the solid phase to the liquid phase due to factors such as mismatched photons, weak pairing within the atomic matrix and decreased uniformity across the photons (Chaichan et al., 2015). Fig. 24 displays the thermal conductivity drop of the RT27 modelled. The thermal conductivity values displayed in Fig. 24 are then inputted as a piecewise linear function with respect to temperature in the prototyping CFD model further elaborated in Section 5.1

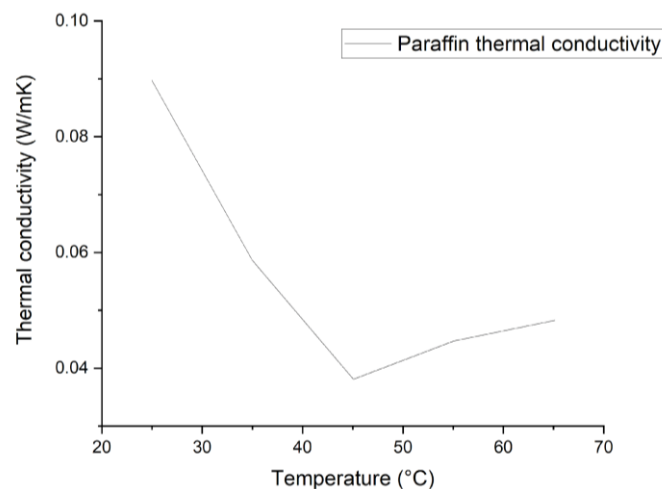


Fig. 24 RT27 thermal conductivity in relation to temperature (Chaichan et al., 2015)

3.2.3 Structure optimization of the final PCM model

Upon establishing both the Li-ion battery heat generation model and the PCM's thermophysical properties, the corresponding parameters were integrated into the final prototype CFD model for optimization. To reduce the weight of the final structure and to conduct heat away from the battery more efficiently, the number of fins, fin thickness and the width of the model is parameterized. It is hypothesized that by increasing the number of fins, expanding the fins' thickness and increasing the width of the model, the amount of heat that can be conducted away from the battery will simultaneously rise to a certain limit. This limit is deduced to be the conclusive prototype structure as it is the most compact structure that is still able to substantially conduct heat away from the battery. Greater detail on the formulation of the Li-ion heat generation model and the optimization process of the prototype is described in Sections 4 and 5, respectively.

4. Results: Battery Thermal Characteristics

Using the heat generation rate equation (Equation 2) established in Section 3 as a function of both joule heating and reversible heating effects, a curve characterisation function was formulated and revised in this section. The curve characterisation function is required as a User Defined Function (UDF) input for the heat generation model in CFD. Within this study, the heat generation of a standard lithium-ion battery was modelled. Thermophysical properties of the Li-ion battery were based off the NCR18650B model. The heat generation plot generated through experimental data by Gümüßsu et. al. (Gümüßsu et al., 2017) was used as a reference in determining the main heat generation equation for the UDF. Firstly, the heat generation values of the battery at 1.0C discharge were modelled using polynomial, exponential and power equations with the Origin2019B mathematical software. Derived functions were then used as transient heat sources under a natural convection CFD model. Transient temperature rises of the battery modelled through the varying UDFs were then compared again with Gümüßsu et. al.'s (2017) experimental values. The function with the smallest deviations in temperature from the experimental values were then scaled for 0.5C and 1.5C discharge rates.

4.1 Function type and battery heat generation CFD settings

4.1.1 Polynomial function

Considering the scalability of a polynomial function, it may be adapted to represent the intricacies of the battery heat generation model. In general, polynomial equations are modelled as shown in Equation 5 below,

$$\dot{Q} = a_0 + a_1t + a_2t^2 + \dots + a_nt^n \quad (5)$$

Whereby \dot{Q} (W/m^3) is the heat generation rate, $a_0 - a_n$ are coefficients corresponding to the polynomial fitting method and t (sec) is the time passed.

4.1.2 Exponential function

A notable characteristic of the battery's heat generation as it nears 0 SOC is its exponentially large increase in heat. Thus, it may be practical to model the heat generation function using an exponential equation as shown in Equation 6.

$$\dot{Q} = \dot{Q}_0 + a_1 e^{t/b_1} + a_2 e^{t/b_2} \quad (6)$$

Whereby \dot{Q} (W/m^3) is the instantaneous heat generation rate, \dot{Q}_0 (W/m^3) is the initial heat generation rate, a_1, a_2, b_1 and b_2 are coefficients corresponding to the exponential model, t (sec) is the time passed. It should be noted that \dot{Q}_0 varies according to both the C-rate and capacity of the battery.

4.1.3 Power function

Similar to exponential functions, power functions share similar characteristics whereby they are able to quantify the notable rise in heat generation towards the end of the discharge cycle.

The power function may be modelled in Equation 7 as follows.

$$\dot{Q} = \dot{Q}_0 + a_1 |t - tc|^p \quad (7)$$

Where \dot{Q} (W/m^3) is the heat generation rate, \dot{Q}_0 (W/m^3) is the initial heat generation rate, a_1, tc and p are coefficients corresponding to the power model and t (sec) is the time passed.

4.1.4 Root mean square error

To determine the accuracy of the heat generation model, Equations 5, 6 and 7 are introduced as heat source functions in the CFD model under the pre-sets described in Section 4.1.5. The maximum temperatures generated by the CFD model are then compared with temperature rise values obtained by Gümüşsu et. al. (2017). There are several statistical means of determining data accuracy including the Mean Absolute Error (*MAE*), Mean Absolute Percentage Error (*MAPE*) and Root Mean Square Error (*RMSE*) methods (J. Willmott and Matsuura, 2005; Kim and Kim, 2016). The practicality of each are debated in numerous studies where some such as Willmott and Matsuura (2005) state that the MAE method is a better metric for measuring average error while Chai and Draxler (2014) highlights that the RMSE method is appropriate for highlighting error distribution in statistical data due to its sensitivity to maximum and minimum errors. Thus, the RMSE method was used as it allows error values to be more quantitatively assessed (Gümüşsu et al., 2017). The RMSE formula is written in Equation 8 below as,

$$RMSE = \sqrt{\frac{1}{n} \sum (T_{CFD} - T_{lit})^2}. \quad (8)$$

Whereby, T_{CFD} are the CFD generated temperatures, T_{lit} are the experimental temperatures obtained from the literature and n is the number of temperature pairs compared.

4.1.5 Battery heat generation CFD settings

The initial settings for all the CFD simulations in this chapter include a heat transfer coefficient of $10 \text{ W/m}^2\text{K}$ and a free stream temperature of 25°C to mimic standard room conditions under natural convection. The dimensions of the NCR18650B battery modelled have a diameter of 18.2 mm and a height of 65 mm as displayed in Fig. 25 (a). The heat source produced across the model stems from the centre of the battery as displayed in Fig 25. (b).

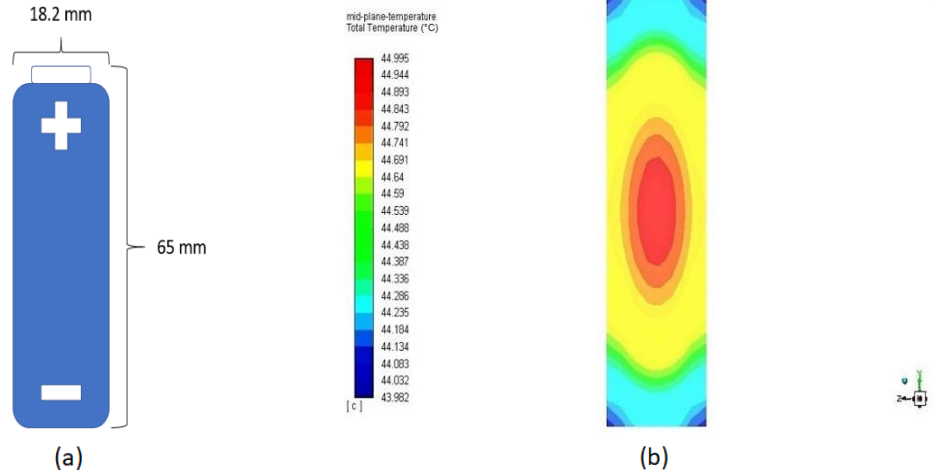


Fig. 25 (a) Geometrical dimensions of the NCR 18650 battery modelled (b) Battery model temperature distribution at $t = 3600s$ after discharging

Thermophysical properties of the battery are based on literature values and are described in Table 5 (Catherino, 2015; Gümüŝsu et al., 2017).

Table 5 Battery thermophysical properties (Catherino, 2015; Gümüŝsu et al., 2017)

Thermophysical properties	Battery	Reference
ρ (kg/m ³)	2939	Gümüŝsu et. al.
c_p (J/kg K)	2400	Catherino
k (W/mK)	3	Catherino

With the intent of ensuring mesh reliability and accuracy, a grid independence study was conducted in relation to the maximum temperature rise of the battery. Mesh sizes of 2.5 mm, 2.0 mm, 1.5 mm and 1.0 mm were modelled for the grid independence study as mesh 1, 2, 3 and 4 respectively. A predominately hexahedral mesh type was selected. The battery's thermophysical properties were set as described in Table 5 and the heat generated was based on a discharge rate of 1.0C. The CFD simulation was set to run at 3600 time-steps to mimic a

one-hour discharge test at 1000 iterations each. The temperature rise of the battery for the varying mesh sizes are graphed in Fig. 26.

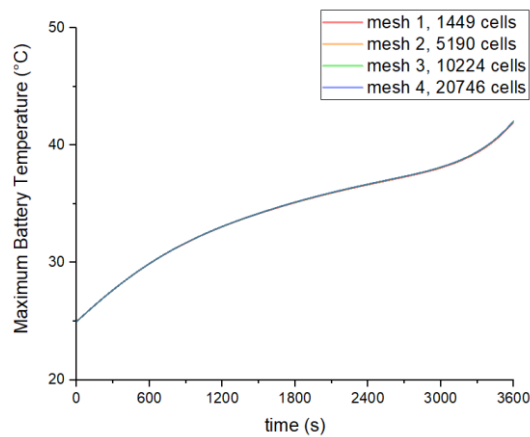


Fig. 26 CFD grid independence study to investigate the effect of varying mesh sizes on temperature rise, based on a battery discharge rate of 1.0C for a duration of 3600s. The overlapping lines indicate that mesh size did not significantly affect the rate of temperature rise.

As shown in Fig. 26, the temperature rise graph did not differ significantly when mesh size was varied. Thus, it can be noted that the increase in the number of cells did not significantly alter the temperature rise of the battery. Hence, mesh 1 was used for further simulations as it required the least amount of computational power while maintaining relevant results.

4.2 Heat generation function

The heat generation functions were determined using the mathematical software Origin 2019b (OriginLab, 2019). A function was deemed fitted when the R-square value was at least 0.9, indicating sufficient accuracy of the function. (Cheng et al., 2014).

4.2.1 Polynomial function

Polynomial functions with different numbers of coefficients ($n = 3, 4, 5, 6$ and 7) were fitted using Origin 2019b (OriginLab, 2019), and then compared against heat generation values obtained from literature (Gümüŝsu et al., 2017) as shown in Fig. 27 below. It should be noted that while increasing the number of coefficients in a polynomial function reduces error, as the function is better able to fit the data, it also runs the risk of overfitting. Thus, it is important to balance between reducing error and overfitting the function.

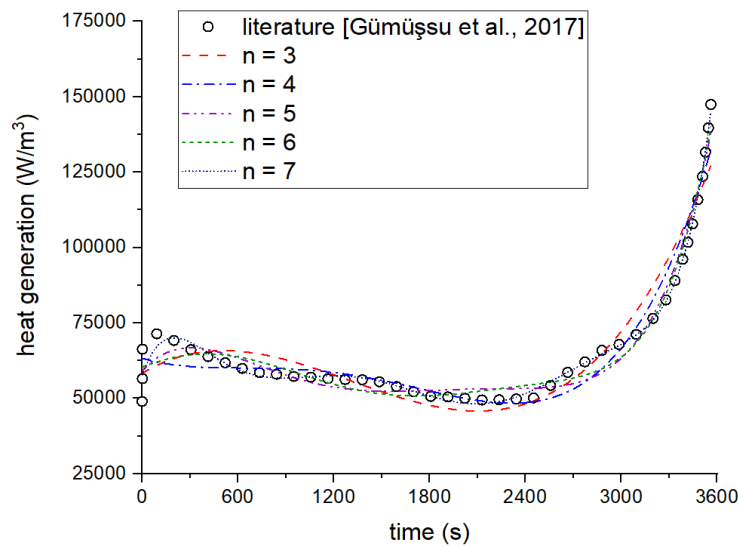


Fig. 27 Polynomial eq. (5) heat generation values at 1C discharge

The coefficients of the fitted polynomial functions are tabulated below as shown in Table 6. These values may be used for the heat generation function of a battery discharging at 1.0C. The suitability of these functions is later assessed and compared against the exponential and power functions in section 4.3.

Table 6 Coefficients for the polynomial heat generation values

N	a0	a1	a2	a3	a4	a5	a6	a7
7	57681.94	152.02	-0.62	9.68E-4	-7.58E-7	3.12E-10	-6.46E-14	5.31E-18
6	60406.18	19.16	-0.01	-4.25E-5	4.46E-8	-1.57E-11	1.90E-15	-
5	59116.31	58.03	-0.14	1.10E-4	-3.75E-8	4.68E-12	-	-
4	63287.74	-15.66	0.03	-1.99E-5	4.19E-9	-	-	-
3	58349.23	31.84	-0.04	9.92E-6	-	-	-	-

4.2.2 Exponential function

The mathematical software Origin 2019b (OriginLab, 2019) was used to fit an exponential function to the heat generation data published by Gümüŝsu et. al. by optimizing the constants a_1 , b_1 , a_2 and b_2 of the exponential function (Gümüŝsu et al., 2017). \dot{Q}_0 is the initial heat generation value, while a_1 , b_1 , a_2 and b_2 are constants that determine the gradient of the function.

Fig. 28 displays the exponential function fitted for the heat generation data. While the function is able to capture the general shape of the referenced heat generation data, it is not able to adequately model the sharp increase in heat generation observed during the beginning of the discharge process. This is due to the rigidity of a typical exponential function. As such, exponential functions are not suitable to fit data points that fluctuate greatly in value.

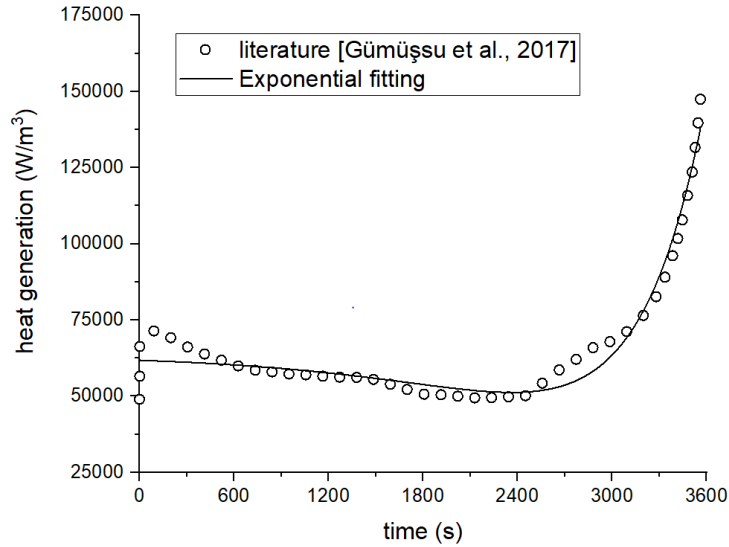


Fig. 28 Exponential heat generation curve eq. (6) values at 1C discharge

Coefficients for the fitted exponential function are displayed in Table 7 below. Similar to the coefficients in Table 6, the values may be used for the transient heat source equation of a typical Li-ion cell.

Table 7 Exponential coefficients

\dot{Q}_0	a_1	b_1	a_2	b_2
63518.40	104.64	478.02	-1833.72	879.12

4.2.3 Power function

A power law function was fitted to the heat generation data published by Gümüşsu et. al. using the Origin 2019b software (OriginLab, 2019, Gümüşsu et al., 2017). Similar to the exponential model presented in Section 4.2.2, the function only manages to capture the general shape of the referenced heat generation but fails to model the sharp rise at the beginning of the energy discharge. The only notable difference is the stabilization of heat generation during the nominal voltage period of the battery. Table 8 displays the coefficients of the power function fitted. The

suitability of this power function to model the heat generation data is assessed and discussed in Section 4.3.

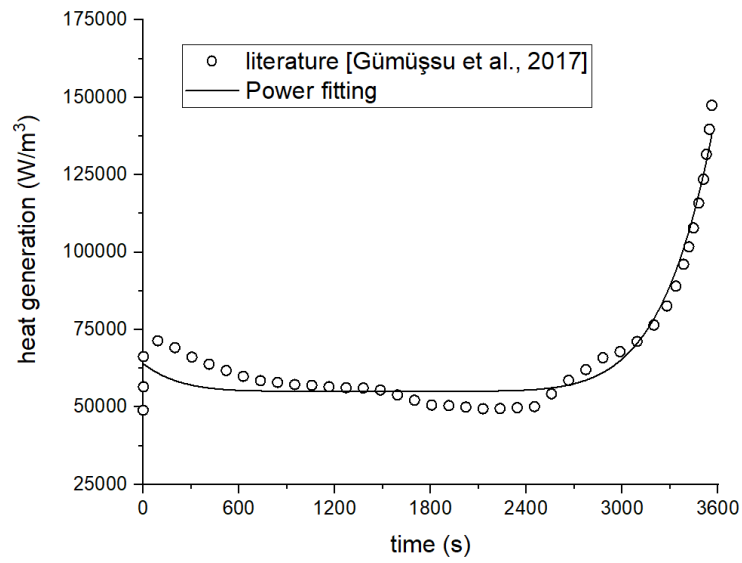


Fig. 29 Power heat generation curve values at 1C discharge

Table 8 Power function coefficients

\dot{Q}_0	a	tc	b
55107.38	1.15E-17	1481.84	6.59

4.3 RMSE values

The heat generation functions modelled in Figs. 27, 28 and 29 were modified and used as User Defined Functions (UDF's) in further CFD models to model the rise in maximum temperature of a battery discharged at 1.0C over time. The maximum temperature rise of the battery in CFD models derived from the polynomial, exponential and power heat generation functions were then compared with the experimental data from Gümüşsu et. al. (Gümüşsu et al., 2017) to calculate the RMSE values as a measure of the model's accuracy as displayed in Fig. 30 (a) and Fig. 30(b) below.

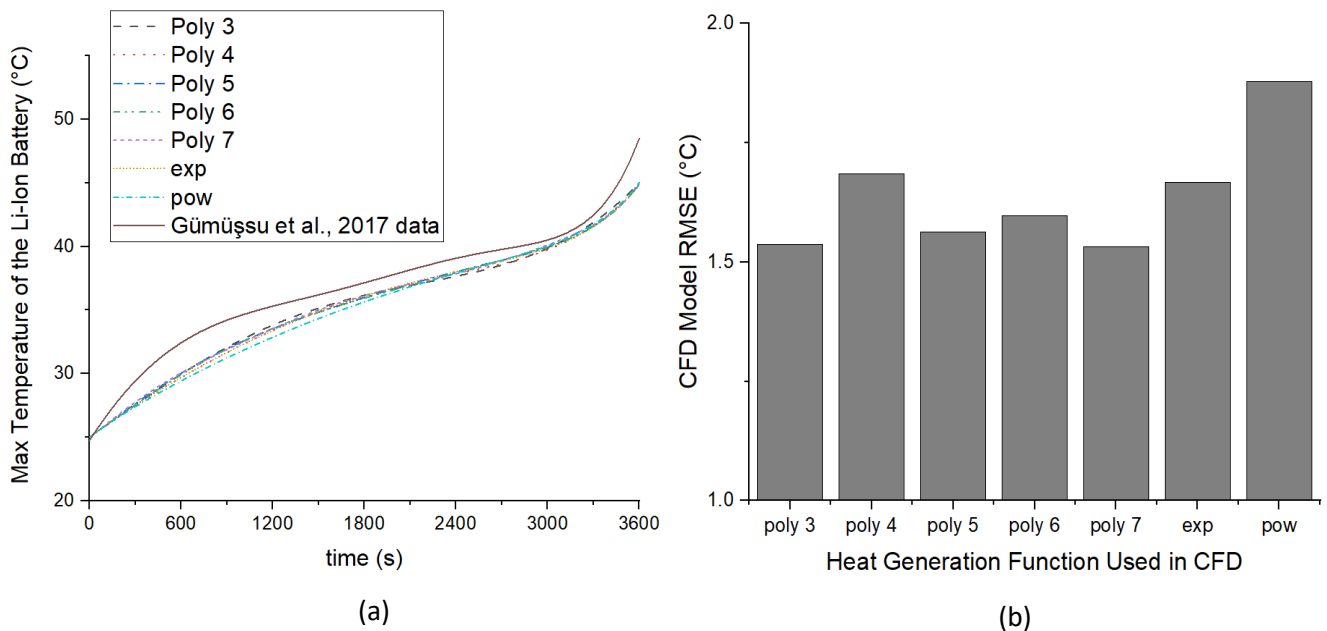


Fig. 30 RMSE method of determining UDF accuracy (a) Max temperature rise of the Li-Ion battery modelled in CFD (b) Comparison of the RMSE values for the various CFD models derived from polynomial, exponential and power heat generation functions at 1C Discharge

By calculating the RMSE, it was noted that the average error in output temperature values of our models at a 1.0C discharge rate ranged from 1.5°C to 1.9°C. While the initial presumption was that an increase in polynomial number would increase the accuracy of the polynomial CFD

models, it was observed that the RSME values did not linearly decrease with the increase in polynomial number. Thus, for polynomial based CFD models with similar RMSE values, it is better to use the model with the lower number of polynomial coefficients to reduce the likelihood of overfitting while preserving the model's accuracy.

It was also observed that the CFD models derived from the exponential and power functions have higher RMSE values compared to the models derived from polynomial functions, indicating that both functions are not as accurate. Such inaccuracies are expected, as it has been observed earlier that the exponential and polynomial functions could not adequately model the sharp initial jump in heat generation during the battery discharge process.

Errors can also be attributed to the fact that Bernardi's heat generation equation, which was used in the CFD models, (Bernardi et al., 1985) was only meant as an approximation of the battery's heat generation. Therefore, modelling the battery's heat generation using Bernardi's equation would have some inaccuracies.

Additionally, another source of error can arise as a result of how the temperature rise was measured - the experimental temperatures measured by Gümüssu et. al. (2017) were taken along the surface of the battery while the temperatures measured in our CFD models were from the centre of the battery.

To better illustrate the deviation in temperature between our CFD models and the experimental values from Gümüssu et. al. (2017), a graph was plotted as displayed in Fig. 31.

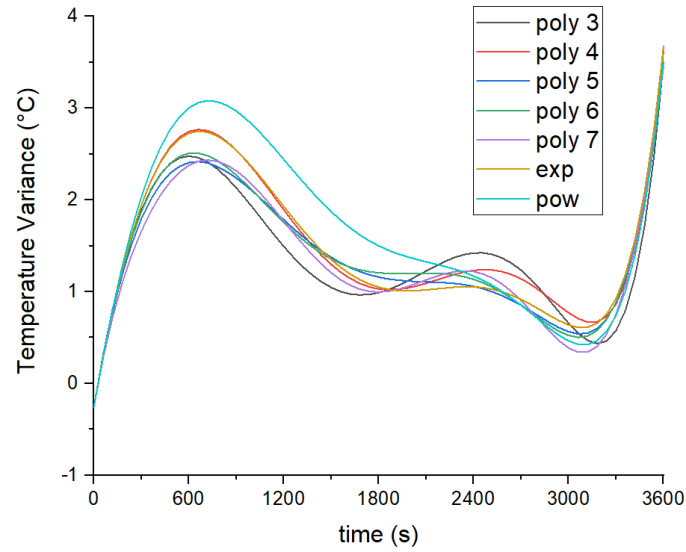


Fig. 31 Temperature deviation between the temperature rise obtained from our CFD models based on various heat generation functions, versus the experimental values reported by Gümüssu et. al. (2017) for a battery discharged at a rate of 1C for a duration of 3600s

Nevertheless, our error margins remain within an acceptable range, especially for the polynomial based CFD models. For comparison, Gümüssu et. al. (2017) reported average error margins of up to 2.0°C across their varying discharge tests and the RMSE values of our heat generation models do not exceed 2.0°C. As the 7th order polynomial function has the lowest RMSE value of 1.5°C, it is thus used as the main UDF for the battery heat generation model.

4.4 Comparison of battery heat generation CFD results

The battery heat generation was modelled as 7th order polynomial functions for the remaining discharge rates as displayed in Fig. 32 below. It was noticed that the troughs at the lower discharge rates were less pronounced compared to those at higher discharge rates. These characteristics corroborate the patterns of heat generation rates reported in literature (Agwu et al., 2018; Liu et al., 2014) as observed by the drop in heat generation values as the battery approaches its nominal capacity and the exponential rise in heat generation as it reaches the end of the discharge cycle. This highlights the large difference between the open circuit voltage and the nominal voltage (Al Hallaj et al., 1999b). Coefficients of the polynomial functions modelled are displayed in Table 9 below.

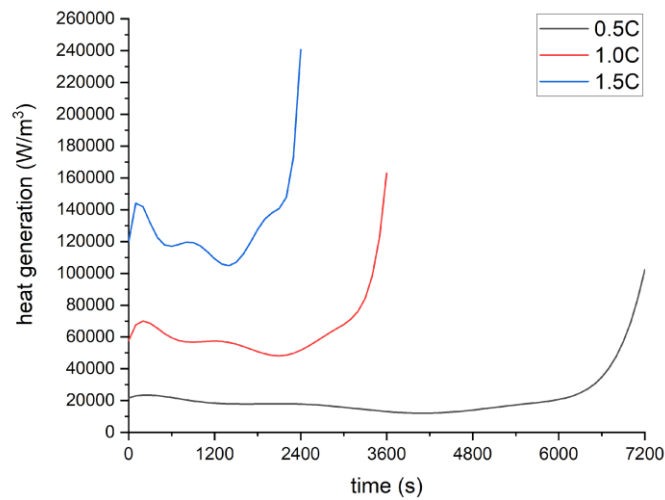


Fig. 32 Seventh order polynomial function heat generation values

Table 9 Coefficients of the 7th order polynomial function used in 3-D CFD modelling of the thermal behaviour of a Li-Ion battery at various discharge rates.

Discharge rate	a0	a1	a2	a3	a4	a5	a6	a7
0.5C	21712.10	16.88	-0.05	4.39E-5	-1.91E-8	4.29E-12	-4.77E-16	2.08E-20
1.0C	57681.94	152.02	-0.62	9.68E-4	-7.58E-7	3.12E-10	-6.46E-14	5.31E-18
1.5C	119986.99	465.10	-2.84	0.01	-7.73E-6	4.72E-9	-1.45E-12	1.76E-16

Upon determining the heat generation functions, they were then used as input into the CFD models for battery temperature increase during discharge, and their results were compared with the experimental values reported by Gümüŝsu et. al. (Gümüŝsu et al., 2017) as highlighted in Fig. 33.

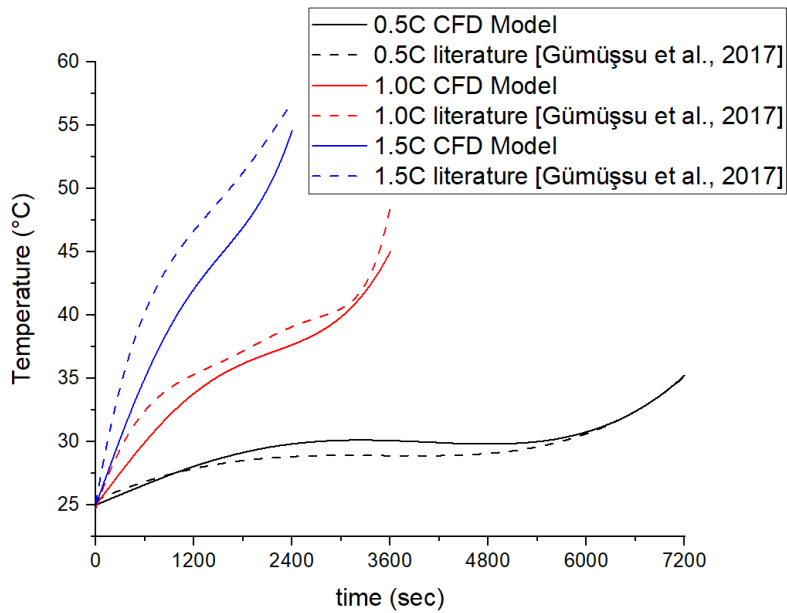


Fig. 33 CFD modelled battery temperatures at versus experimental values reported by Gümüŝsu et. al. at various discharge rates (Gümüŝsu et al., 2017)

There appears to be a good fit for the battery temperatures at the 0.5C and 1.0C discharge rates, with a standard deviation in temperature of $-0.47^{\circ}\text{C} \pm 0.8^{\circ}\text{C}$ and $1.36^{\circ}\text{C} \pm 1.6^{\circ}\text{C}$ respectively. However, the 1.5C discharge temperature values appear to deviate to a greater extent with standard deviation values of $3.82^{\circ}\text{C} \pm 3.7^{\circ}\text{C}$. Quantitatively, the RMSE values described in Fig. 34 below show that the 1.5C discharge model has an RMSE value of around 4.0°C , which is significantly higher compared to those at 0.5C and 1.0C discharge rates.

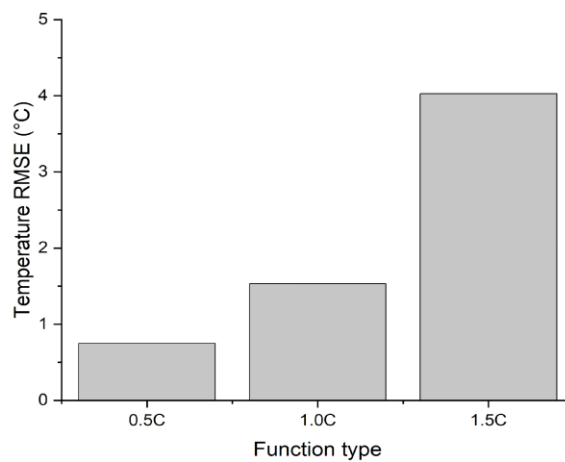


Fig. 34 RMSE values of the battery temperature rise CFD model at 0.5C, 1.0C and 1.5C discharge rates

In conclusion, through the results obtained, it was noted that the seventh order polynomial heat generation function had the best fit compared to the other function types, as its RMSE value was the lowest compared to the other functions. As such, the function was used for the optimization of the onboard PCM thermal management system. Details on the design and optimization process is highlighted in the following chapter.

5. Results: PCM Thermal Management System

The thermophysical properties of the PCM Rubitherm RT27 as identified in Section 3.2.2 and the polynomial heat generation model of the Li-ion battery as determined in Section 4.4 were introduced as input parameters into the optimization process of the final PCM thermal management prototype. The optimization of the PCM thermal management system was conducted by parameterizing both the number of fins within the honeycomb cell and the width of the cell design. The ideal design would minimize the number of fins and the cell width while maximizing the amount of heat conducted away from the battery during the discharge process. Additionally, the prototype was also modelled without the PCM and cooled under natural convection to determine the significance of the PCM in improving the thermal management of the prototype.

5.1 Prototype Design

As previously established in Section 3.1, a hexagonal geometry with a circular core was selected as the design of the prototype model. Benefits from such a design include being able to pack multiple cells without any space wasted in the honeycomb, house adequate quantities of the RT27 within its trapezoidal channels, maintain good structural stability and enhance the thermal conductivity of the RT27. Aluminium was selected as the main housing material due to its high thermal conductivity and relatively economical cost (Royal Society of Chemistry, 2020). To maintain adequate thermal contact and to prevent electrical conduction between the battery and the main aluminium housing, a thermal pad was considered to fill the gap between the battery and the aluminium housing.

Other parameters were also considered but ultimately not integrated when optimizing the thermal efficiency of the prototype. Parameterization of fin thickness was not considered as

studies conducted by Al-Abidi et al. (Al-Abidi et al., 2013) highlighted that an incremental increase in fin thickness by 1mm only reduces the melting time of PCM by an average of 2.8%, which is not significant. Meanwhile, the same study described that incrementally increasing the number of fins reduces the melting time of PCM by an average of 19% for each fin added. Hence, the number of fins attached onto the prototype was parameterized for their effectiveness in reducing the battery's maximum temperature.

An illustration of the prototype model is displayed in Fig. 35 below. Fin thickness was left at 1 mm, the battery was housed at the centre of the circular core to maximize heat transfer to the aluminium fin structure and the thermal pad was positioned between the battery and the prototype to prevent short circuiting while maintaining adequate thermal contact.

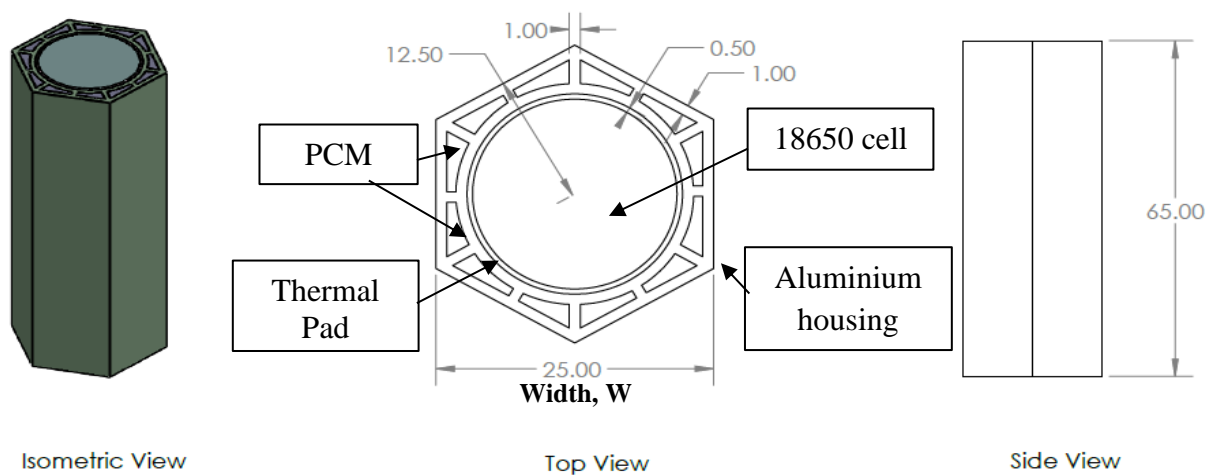


Fig. 35 Concept design of the enhanced PCM passive thermal management system

Subsequently, the model width and PCM volume were further parameterized by increasing the aluminium housing's width by 2.0 mm increments and measuring the model's thermal dissipation effectiveness. The range of the parameterized model widths and PCM volumes is tabulated in Table 10 below.

Table 10 Parameterized values of the prototype constructed in the current study

Model	Width, W (mm)	PCM Volume (mm ³)
1	25.0	5132.95
2	27.0	9696.61
3	29.0	14710.61
4	31.0	20174.93
5	33.0	26089.60
6	35.0	32454.59
7	37.0	39269.92
8	39.0	46535.58
9	41.0	54251.57
10	43.0	62417.90
11	45.0	71034.56

5.2 Structure Parameterization

5.2.1 Model Width Parameterization

The transient heat generation of an NCR18650B Li-ion battery at a 1.0C discharge rate was modelled under natural convection conditions and compared against a battery discharged at the same rate with Model 3 of the PCM system as described in Table 10 above using our CFD model. Model 3 was selected as a sample to illustrate the comparison between the rise in temperature of the Li-Ion battery with and without the system. The heat transfer coefficient of both models was set at $10 \text{ W/m}^2\text{K}$ to mimic natural convection conditions (Kosky et al., 2013, p. 12). The results as displayed in Fig. 36 and Fig. 37 below indicate that the system reduces the overall temperature of the battery by an average of 6.79°C throughout a 1.0C discharge cycle.

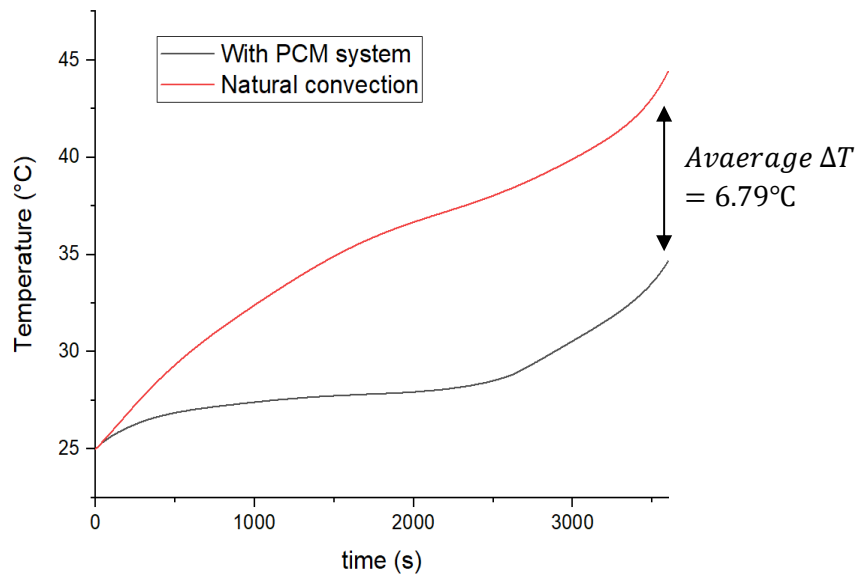


Fig. 36 Comparison between a natural convection system and Model 3, $W = 29.0\text{mm}$ at a 1.0C discharge rate for a duration of 3600s

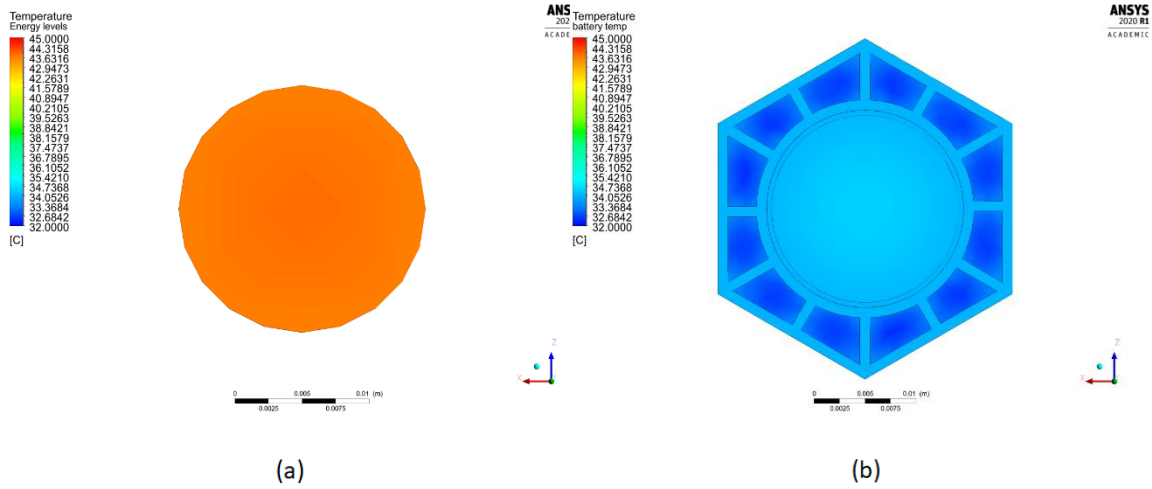


Fig 37 Comparison of the thermal distribution of an NCR18650B Li-ion battery at a 1.0C discharge rate after 3600s, cooled under: (a) Natural convection (b) A PCM passive BTM system, Model 3, $W = 29.0 \text{ mm}$

To further explore the effectiveness of increasing both model width and the volume of PCM used, the remaining models were subjected to the heat generation of the battery at a 1.0C discharge rate and the battery's corresponding T_{Max} was observed as illustrated in Fig. 38.

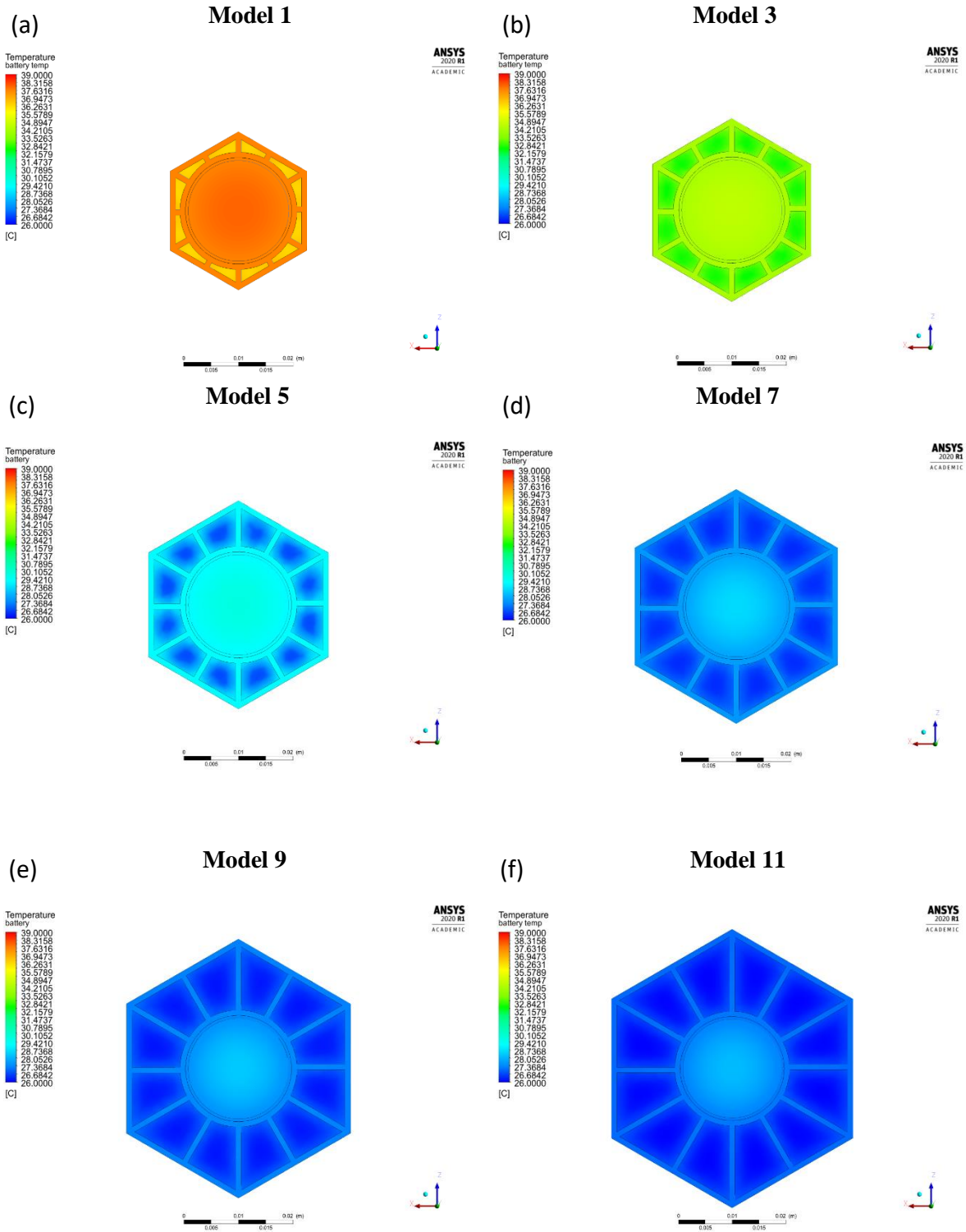


Fig. 38 Model width and PCM volume parameterization battery temperature at 3600s after discharge at a rate of 1.0C

(a) Model 1 (b) Model 3 (c) Model 5 (d) Model 7 (e) Model 9 (f) Model 11

From the results shown in Fig. 38, it was observed that by incrementally increasing the width of the model and the PCM volume used, the maximum core temperature of the battery was increasingly reduced. Table 11 displays the maximum temperature rise of the various models after 3600s at a 1.0C discharge rate.

Table 11 Max temperature rise of the Li-ion battery after 3600s at a 1.0C discharge rate for the different models

Model	1	2	3	4	5	6	7	8	9	10	11
Li-ion battery max temp rise (°C)	13.26	11.73	9.66	6.07	4.99	4.04	3.70	3.62	3.44	3.31	3.22
Width of the model (mm)	25.0	27.0	29.0	31.0	33.0	35.0	37.0	39.0	41.0	43.0	45.0

Fig. 39 displays the transient temperature rise of the battery at a 1.0C discharge rate for Model 1 to Model 11 as described in Table 11. It was noted that the drop in the battery's maximum temperature becomes less significant ($< 1^{\circ}\text{C}$) beyond Model 6. As space is a premium within a battery pack, Model 6 appears to be the most appropriate iteration to be used.

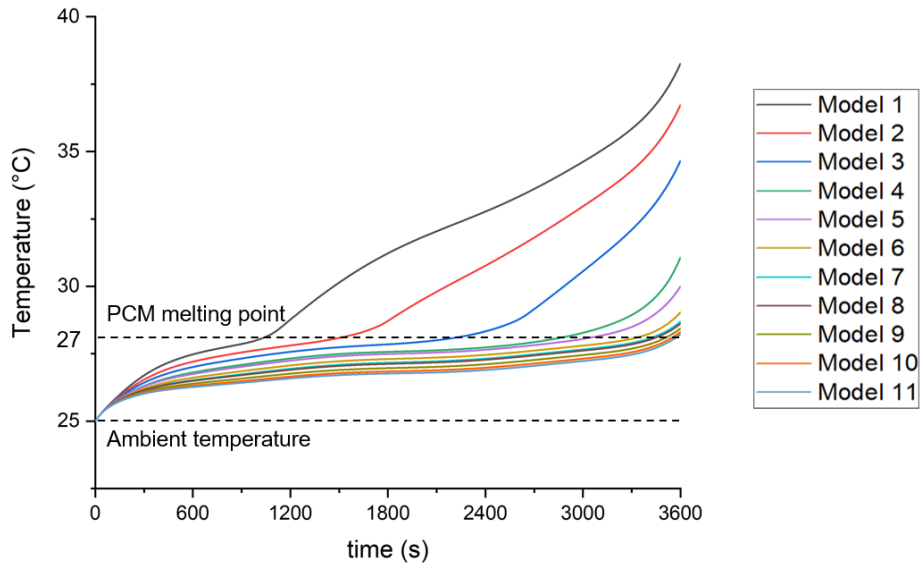


Fig. 39 Temperature rise of the battery in response to increasing the width of the model over the course of 3600s at a 1.0C discharge rate. Model 6 is the most appropriate model as the reduction in the battery’s temperature rise is not as significant from Model 7 onwards

5.2.2 Fin Number Parameterization

With the ideal model width determined in section 5.2.1, the number of fins in the prototype was further parameterized by incrementally increasing the fin number from 4 to 14, as presented in Fig. 40. To ensure even heat distribution across the RT27, the fins were evenly spaced apart in the prototype model.

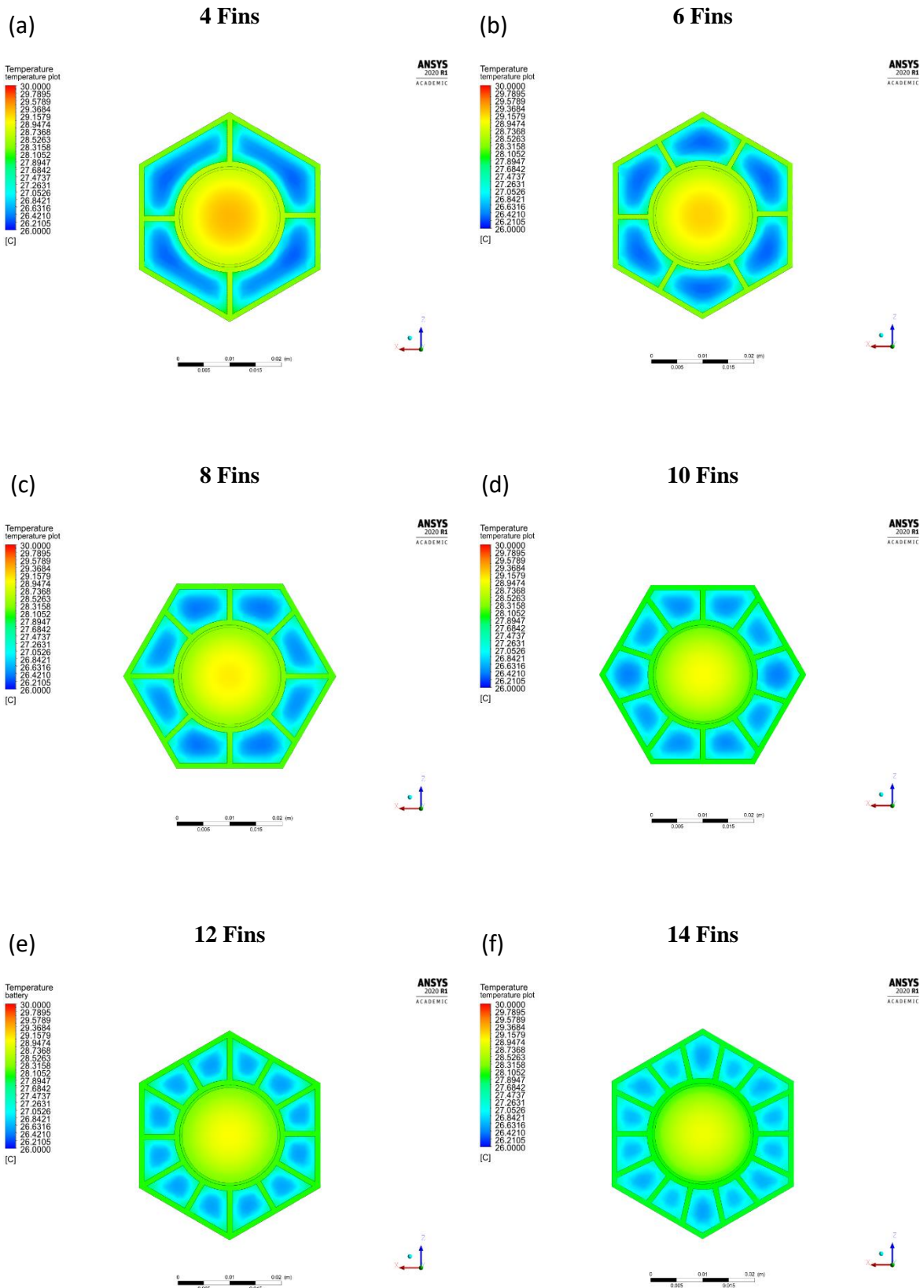


Fig. 39 Fin number parameterization with cell width, $W = 35\text{mm}$ at $t = 3600\text{s}$ at a 1.0C discharge rate (a) 4 fins (b) 6 fins (c) 8 fins (d) 10 fins (e) 12 fins (f) 14 fins

The transient temperature rise of the Li-Ion batteries is shown in Fig. 40 below. Notably, the effects of increasing the number of fins in lowering the battery's T_{max} was not very significant as compared to increasing the model width.

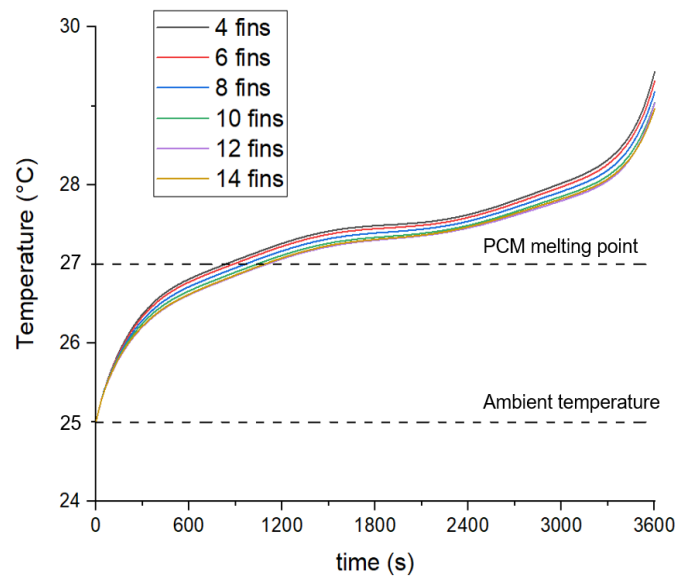


Fig. 40 Transient battery temperature rises with respect to increasing the number of fins for $t=3600s$ at a 1.0C discharge rate.

Table 12 displays the maximum temperature rise of the Li-Ion battery after 3600s at a 1.0C discharge rate for the models with varying fins. On average, between the range of 4 fins to 10 fins, initially incrementally increasing the number of fins by 2 in the prototype lowers the battery's T_{max} by $0.14^{\circ}C$. However, from the 10-fin model onwards there was only an average change of $0.04^{\circ}C$ in T_{max} ($\Delta T_{Max} = 0.04^{\circ}C$). As such, the 10-fin model was chosen as ideal as to reduce the weight of the system while maintaining adequate cooling.

Table 12 Max temperature rise of the Li-ion battery in a $W=35mm$ cell after 3600s at a 1.0C discharge rate for different numbers of fins

Number of fins	4	6	8	10	12	14
Li-ion battery max temp rise ($^{\circ}C$)	4.43	4.32	4.18	4.04	4.04	3.96

5.2.3 Comparison of the system with/without PCM

The thermal dissipation difference between the battery system with and without the RT27 is then modelled to determine the significance of the PCM across in the prototype design in terms of lowering the maximum battery temperature. Discharge parameters are set similarly to the conditions set in Sections 5.2.1 and 5.2.2, with the batteries being discharged at a rate of 1.0C under natural convection conditions.

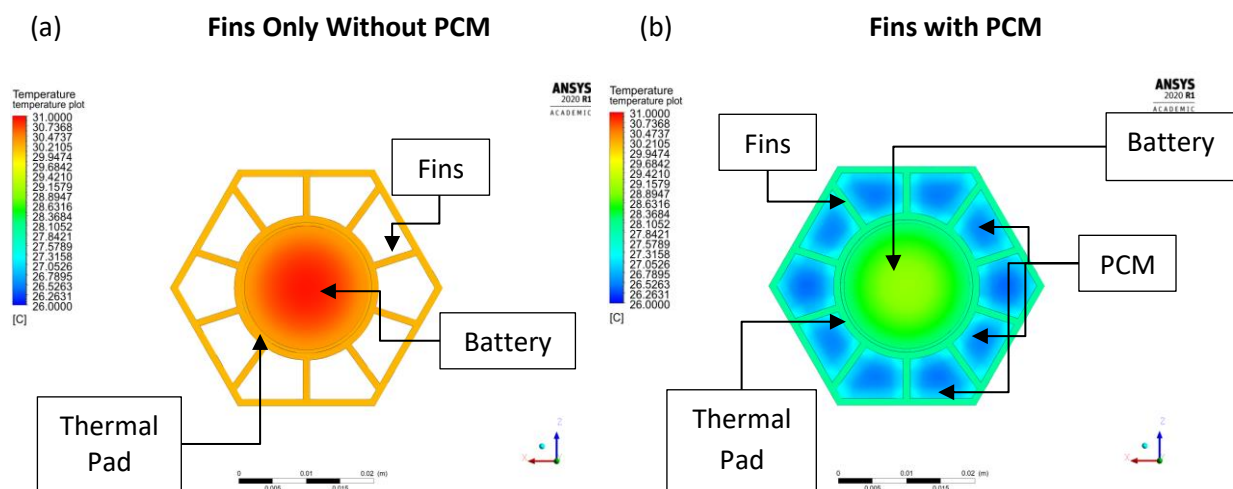


Fig. 41 Comparison of the temperature distribution of the finned prototype system with/without the PCM at $t=3600s$ discharged at 1.0C (a) Prototype model without PCM (b) Prototype model with PCM

As displayed across Fig. 41, the presence of the PCM significantly lowers the battery's maximum temperature at the end of the discharge phase.

The parameterization was then repeated at a higher discharge rate of 2.0C to investigate the significance of the RT27 at different discharge rates. As shown in Fig. 42 below, the effectiveness of the PCM is more pronounced at higher discharge rates. When the battery was

discharged at 1.0C, T_{max} (°C) of the battery system after 3600s with and without the PCM was 29.04°C and 31.03°C respectively ($\Delta T_{max} = 2.00^\circ\text{C}$). At a 2.0C discharge rate after 1800s, the T_{max} of the battery system with and without the PCM was 32.60°C and 36.52°C respectively ($\Delta T_{max} = 4.00^\circ\text{C}$). Thus, batteries charged at higher discharge rates benefit more from incorporating the PCM in the BTM prototype. The transient temperatures of the battery with the finned only and the finned PCM model discharged at 1.0C and 2.0C rates are shown in Fig. 42 below.

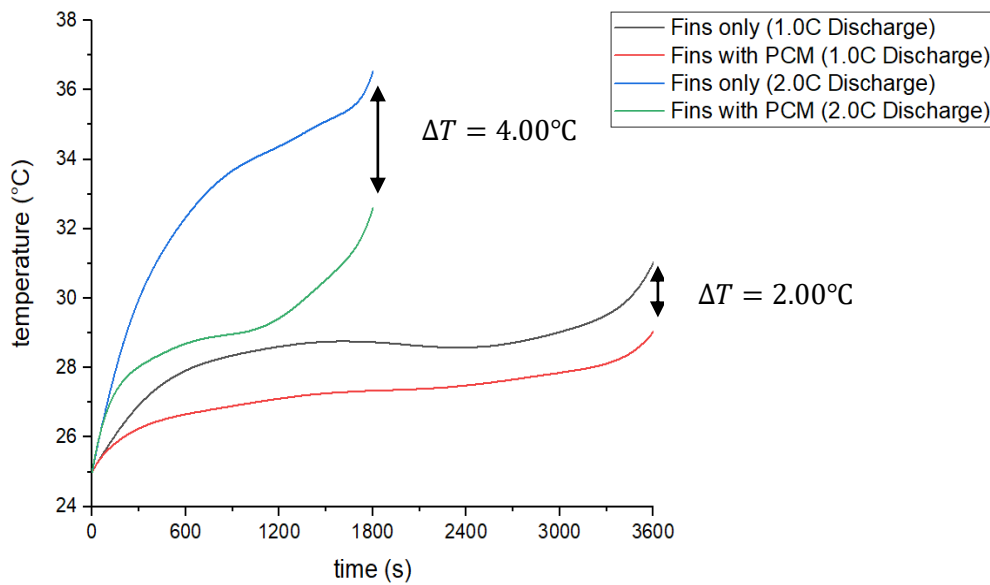


Fig. 42 Temperature rise of the finned system with/without the PCM at a 1.0C and 2.0C discharge rate through a duration of 3600s and 1800s, respectively.

5.2.4 Varying ambient temperature

The optimized PCM BTM prototype consisting of 10 fins and a width of 35.0mm as shown in Fig. 43 was then modelled under various ambient conditions and discharge rates. This was conducted to determine the influence of the ambient temperature on the prototype's effectiveness.

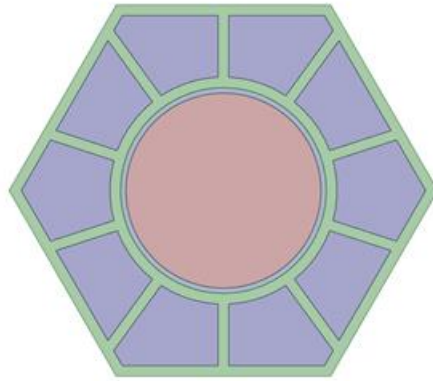


Fig. 43 Optimized PCM battery thermal management model consisting of 10 fins with a width of 35.0 mm

As shown in Fig. 44 below, at an ambient temperature of 15°C, the prototype was able to limit the battery's temperature rise at the end of the discharge cycle to approximately 12.0°C at both 1.0C and 2.0C discharge rates. At a 3.0C discharge rate, the battery's temperature rise at the end of the discharge cycle was 16.48°C. It should be noted that the battery's rate of temperature rise decreases as T_{Bat} reaches beyond the paraffin's melting point of 27°C. This is due to the increased amount of energy required to overcome the latent heat of the paraffin's phase change as the battery approaches that temperature.

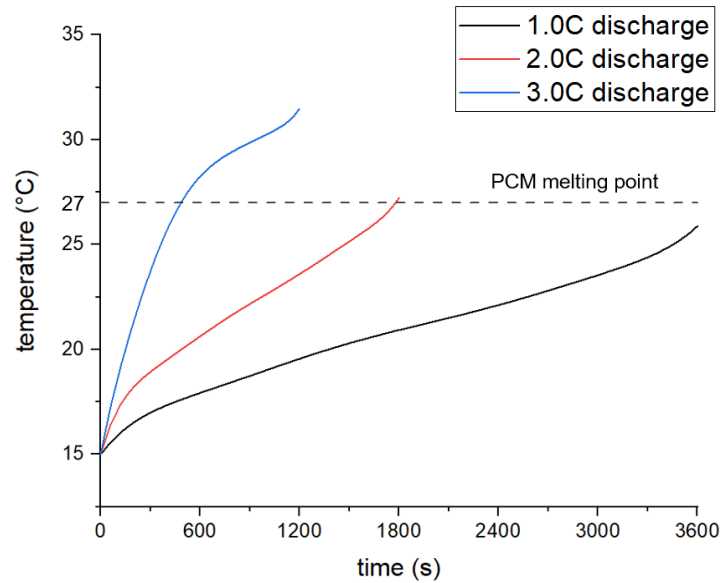


Fig. 44 Maximum temperature rise of the battery within the PCM thermal management prototype at 15°C ambient temperature

The battery's temperature rise in the PCM prototype was also modelled at an ambient temperature of 25°C as shown in Fig. 45. It can be observed that as the battery's temperature goes beyond the melting temperature of the PCM, the temperature rise is greatly reduced. When the discharge rate is at 1.0C, the temperature rise of the prototype increases by 4.10°C. Such values are significantly lower as compared to the temperature rise of the battery when the ambient temperature is at 15°C. Similarly, low temperature rises are displayed for 2.0C and 3.0C discharge rates with temperature rises of 7.60°C and 10.10°C occurring across the battery

respectively. Such data show that the prototype could perform exceptionally well across most equatorial climates as temperature around those regions are around 25°C.

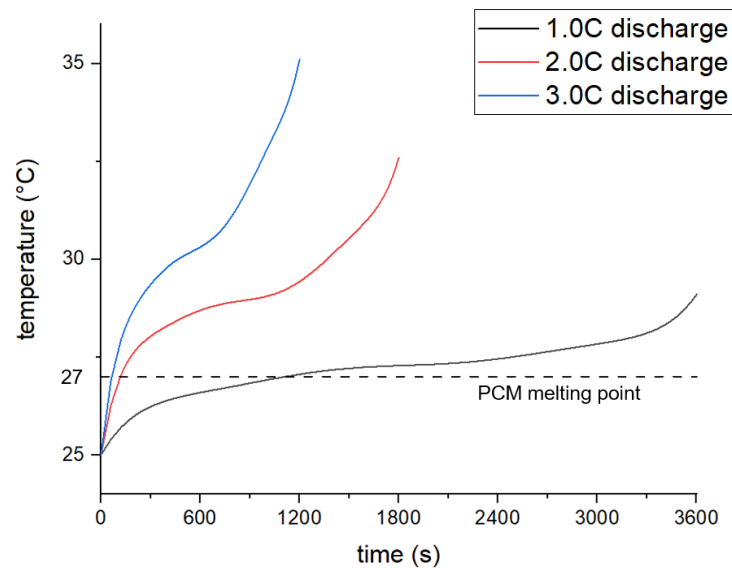


Fig 45 Maximum temperature rise of the battery within the PCM thermal management prototype at 25°C ambient temperature

As the ambient temperature is above the melting point of the PCM, the effectiveness of the prototype drops as highlighted in Fig. 46 where the ambient temperature is simulated at 35°C. The temperature rises of the battery for the 1.0C, 2.0C and 3.0C discharge rates are at 10.39°C, 17.62°C and 21.37°C respectively while ambient temperatures are as such. Thus, it can be deduced that the deployment of the prototype in warmer climates would not be advisable unless the paraffin utilized is replaced with another PCM type with a higher melting point.

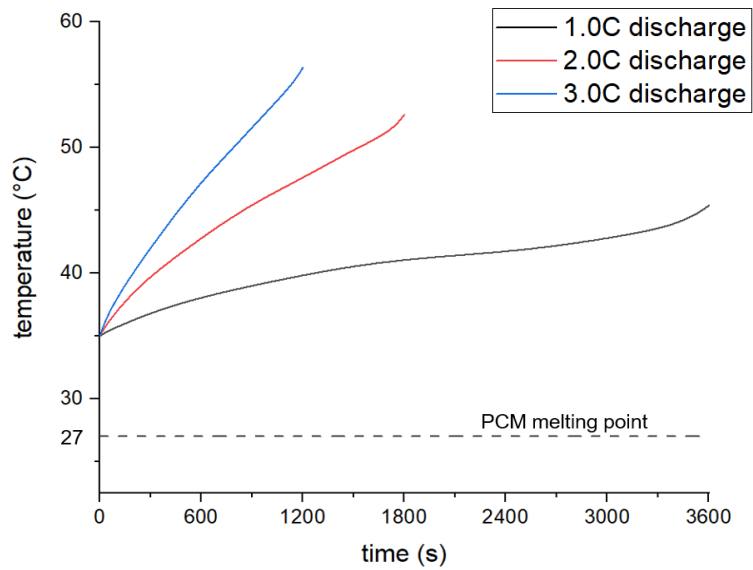


Fig. 46 Maximum temperature rise of the battery within the PCM thermal management prototype at 35°C ambient temperature

A summary of the varying temperature rises at different discharge rates and ambient temperatures are tabulated in Table 13 below. The prototype works optimally in cooling the battery to around 27°C making it ideal for regions with such median temperatures. Higher temperature ranges would require a different PCM type.

Table 13 Temperature rise of the battery at varying ambient and discharge rates

Ambient temperature (°C)	Temperature rise (°C)		
	1.0C discharge rate	2.0C discharge rate	3.0C discharge rate
15	10.88	12.22	16.48
25	4.10	7.60	10.10
35	10.39	17.62	21.37

5.3 Final prototype design

With the optimized structure of the model established, a detailed version of the prototype was then designed as displayed in Fig. 47 below.

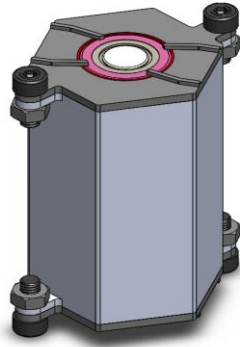


Fig. 47 Assembly of the PCM thermal management design for a single cell

The general assembly consists of the aluminium housing, thermal pad, plastic separator/lid and 4 pairs of M4 nuts and bolts. As previously established, the aluminium housing stores the RT27, enhances its thermal conductivity, and strengthens the structure's design. The thermal pad separates the 18650-battery body from the aluminium housing to prevent a short circuit as well as maintain sufficient heat transfer from the battery towards the prototype. Similarly, the top PLA plastic lid/separator seals the RT27 within the channels of the aluminium housing while separating the aluminium housing from the busbar connections that will be connected at both the anode and cathode of the battery to prevent a short circuit. The bottom PLA plastic lid/separator merely separates the aluminium housing from the busbar connection as the aluminium housing contains a base. This is needed as the risk of PCM leakage is greater at the base of the prototype as compared to the top.

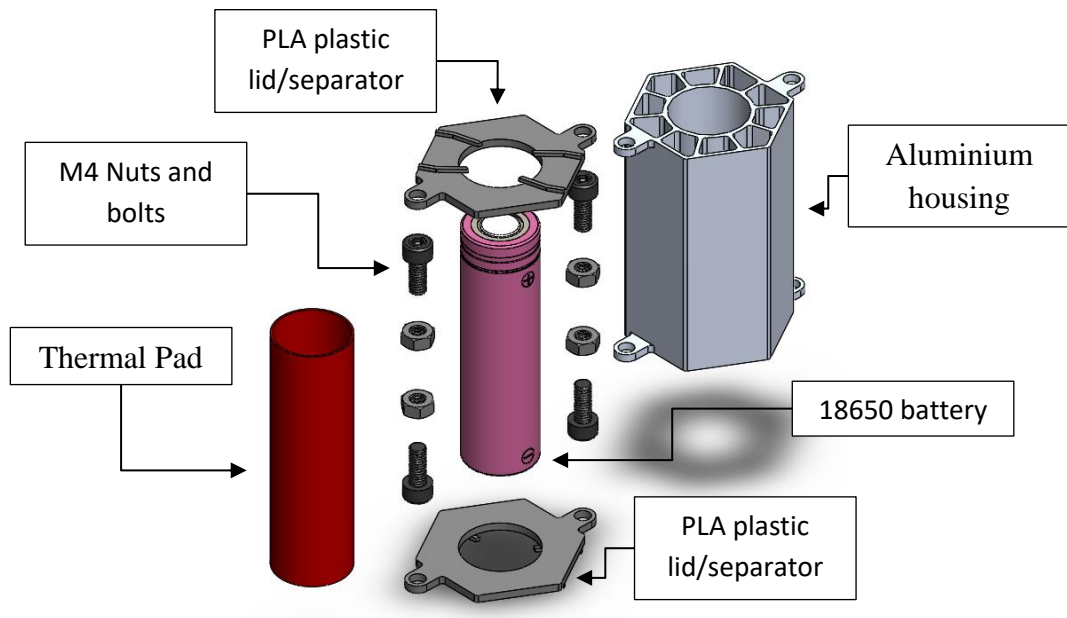


Fig 48 Components of the PCM thermal management design for a single cell

5.4 Future works and recommendations

While the current study has identified through CFD simulation that the prototype is able to cool a standard 18650 battery under varying ambient and discharge conditions, greater improvements on the design and the study itself could have been made. For instance, additional research could be conducted on how the prototype would perform under cold weather conditions as the current study has a greater emphasis on the cooling performance of the prototype. Investigation into the structural strength of the prototype would also be practical in determining the survivability of the prototype under collision circumstances. Additionally, a study on how well the prototype may be scaled in the context of a larger battery pack and the manufacturability of the prototype would have numerous benefits to the commercial viability of the project.

6. Conclusion

With the aim of developing and optimizing a passive PCM thermal management system for EV applications, several objectives were established to fulfil such requirements. The objectives set-out included designing a prototype that can house a standard 18650 battery while simultaneously regulating its temperature, determining the heat transfer rate, \dot{Q} of a typical 18650 cell under varying discharge rates, identifying the most optimal PCM type to be used for Li-ion battery temperature regulation, optimizing the prototype to effectively transfer heat from the battery to the PCM with the smallest volume possible and to measure its effectiveness under varying ambient conditions.

A finned hexagonal honeycomb aluminium structure with a circular central core was designed for the prototype. The geometrical structure was utilized for it had several advantages including being able to house a standard 18650 battery while maintaining sufficient cooling across the battery, store sufficient volumes of PCM within its channels to absorb heat away from the battery, enhance the thermal conductivity of the PCM stored and being structurally strong. The heat transfer rate of the battery is determined to be the best modelled with the 7th order polynomial function as shown in Equation 9. Corresponding coefficients for Equation 9 are based on the discharge rate of the battery.

$$\dot{Q} = a_0 + a_1t + a_2t^2 + \dots + a_nt^n \quad (9)$$

PCM Rubitherm RT27, a type of paraffin was selected as the main PCM component of the prototype as it has a melting point of 27.00°C which is within the optimal temperature range of a standard 18650 battery which is between the range of 15~35 °C. As the RT27 approaches its melting temperature, large quantities of energy are required to overcome its high latent heat capacity allowing the prototype to regulate its temperature around the 15~35 °C range.

Optimization of the prototype was conducted through CFD by parameterizing the number of fins and width length of the model to effectively minimize the battery's temperature rise during the discharge cycle. Generally, increasing the model width led to a larger volume in PCM used while increasing the number of fins increased its thermal conductivity. The effectiveness of incrementing both values diminishes once it reaches its optimal configuration which is 10 fins and a width length of 35mm. As the prototype is simulated under varying discharge and ambient conditions, it is identified that the model is able to handle discharge rates of up to 3.0C but only if ambient conditions do not exceed 27°C signifying that the prototype is best used in equatorial and cold climates.

Greater improvements can be made to both the prototype's design and how the study was conducted. Examples of further works that could be conducted include improving the design to regulate the battery for colder climates, scaling the honeycomb cell for pack level design and improving the manufacturability of the prototype. More accurate CFD models could also be implemented to improve the model's accuracy. Nevertheless, future iterations of the prototype would surely aid in the progression of battery technologies which in turn would ultimately hasten the adoption of electric vehicles in the current market.

7. References

- Advanced Cooling Technologies, 2019. PCM Heat Sink Design Considerations [WWW Document]. URL <https://www.1-act.com/innovations/thermal-storage/pcm-heat-sink-design-considerations/> (accessed 1.10.19).
- Agwu, D.D., Opara, F., Chukwuchekwa, N., Dike, D., Uzoechi, L., 2018. Review Of Comparative Battery Energy Storage Systems (Bess) For Energy Storage Applications In Tropical Enviroments. https://www.researchgate.net/publication/327966044_Review_Of_Comparative_Battery_Energy_Storage_Systems_Bess_For_Energy_Storage_Applications_In_Tropical_Enviroments
- Agyenim, F., Hewitt, N., Eames, P., Smyth, M., 2010. A review of materials, heat transfer and phase change problem formulation for latent heat thermal energy storage systems (LHTESS). *Renew. Sustain. Energy Rev.* 14, 615–628. <https://doi.org/10.1016/j.rser.2009.10.015>
- Al Hallaj, S., Maleki, H., Hong, J.S., Selman, J.R., 1999a. Thermal modeling and design considerations of lithium-ion batteries. *J. Power Sources* 83, 1–8. [https://doi.org/10.1016/S0378-7753\(99\)00178-0](https://doi.org/10.1016/S0378-7753(99)00178-0)
- Al Hallaj, S., Maleki, H., Hong, J.S., Selman, J.R., 1999b. Thermal modeling and design considerations of lithium-ion batteries. *J. Power Sources* 83, 1–8. [https://doi.org/10.1016/S0378-7753\(99\)00178-0](https://doi.org/10.1016/S0378-7753(99)00178-0)
- Al-Abidi, A.A., Mat, S., Sopian, K., Sulaiman, M.Y., Mohammad, A.Th., 2013. Internal and external fin heat transfer enhancement technique for latent heat thermal energy storage in triplex tube heat exchangers. *Appl. Therm. Eng.* 53, 147–156. <https://doi.org/10.1016/j.applthermaleng.2013.01.011>

- Alam, T.E., Dhau, J.S., Goswami, D.Y., Stefanakos, E., 2015. Macroencapsulation and characterization of phase change materials for latent heat thermal energy storage systems. *Appl. Energy* 154, 92–101. <https://doi.org/10.1016/j.apenergy.2015.04.086>
- Al-Saadi, S.N., Zhai, Z. (John), 2015. Systematic evaluation of mathematical methods and numerical schemes for modeling PCM-enhanced building enclosure. *Energy Build.* 92, 374–388. <https://doi.org/10.1016/j.enbuild.2015.01.044>
- Battery University Group, 2020. BU-1003a: Battery Aging in an Electric Vehicle (EV) – Battery University [WWW Document]. URL https://batteryuniversity.com/learn/article/bu_1003a_battery_aging_in_an_electric_vehicle_ev (accessed 9.28.20).
- Battery University Group, 2018. BU-1003: Electric Vehicle (EV) [WWW Document]. batteryuniversity.com. URL https://batteryuniversity.com/learn/article/electric_vehicle_ev (accessed 10.2.18).
- Battery University Group, 2017. Charging at High and Low Temperatures [WWW Document]. URL https://batteryuniversity.com/learn/article/charging_at_high_and_low_temperatures (accessed 6.25.20).
- Bauchrowitz, E., Graf, H., Kessler, F., Lichtenberger, M., 2010. The hybrid drive system in the BMW active hybrid 7. *ATZ Worldw.* 112, 30–36. <https://doi.org/10.1007/BF03225139>
- Bernardi, D., Pawlikowski, E., Newman, J., 1985. A General Energy Balance for Battery Systems. <https://doi.org/10.1149/1.2113792>
- Berthou, Y., 2011. Étude de parois de bâtiments passifs associant un Matériau à Changement de Phase (MCP) et une super isolation transparents (thesis). Paris, ENMP. <https://scanr.enseignementsup-recherche.gouv.fr/publication/these2011ENMP0109>

- Bloomberg, 2020. An Economic Crash Will Slow Down the Electric Vehicle Revolution ...
But Not For Long. Bloomberg.com. <https://www.bloomberg.com/news/articles/2020-03-17/an-economic-crash-will-slow-down-the-electric-vehicle-revolution-but-not-for-long>
- Bower, G., 2018. Tesla Model 3 Battery Cooling Much-Improved ... Track Mode? [WWW Document]. InsideEVs. URL <https://insideevs.com/news/338711/tesla-model-3-battery-cooling-much-improved-track-mode/> (accessed 2.1.20).
- Catherino, H., 2015. An Analysis of Heat Generation in a Lithium Ion Cell. SAE Soc. Automot. Eng. Trans. Catherino, H., "An Analysis of Heat Generation in a Lithium Ion Cell," SAE Technical Paper 2015-01-2420, 2015. <https://doi.org/10.4271/2015-01-2420>
- Chai, T., Draxler, R.R., 2014. Root mean square error (RMSE) or mean absolute error (MAE)? – Arguments against avoiding RMSE in the literature. *Geosci. Model Dev.* 7, 1247–1250. <https://doi.org/10.5194/gmd-7-1247-2014>
- Chaichan, M., H, K., M, A.-A., 2015. Thermal Conductivity Enhancement by using Nano-material in Phase Change Material for Latent Heat Thermal Energy Storage Systems. *SAUSSUREA* 5, 48–55. <https://thermtest.com/papers/thermal-conductivity-enhancement-by-using-nano-material-in-phase-change-material-for-latent-heat-thermal-energy-storage-systems>
- Chang, C., 2019. Factors Affecting Capacity Design of Lithium-Ion Stationary Batteries. *Batteries* 5, 58. <https://doi.org/10.3390/batteries5030058>
- Chen, K.-H., Han, T., Khalighi, B., Klaus, P., 2017. Air Cooling Concepts for Li-Ion Battery Pack in Cell Level. p. V001T09A001. <https://doi.org/10.1115/HT2017-4701>

- Cheng, C.-L., Shalabh, Garg, G., 2014. Coefficient of determination for multiple measurement error models. *J. Multivar. Anal.* 126, 137–152.
<https://doi.org/10.1016/j.jmva.2014.01.006>
- Choi, D.H., Lee, J., Hong, H., Kang, Y.T., 2014. Thermal conductivity and heat transfer performance enhancement of phase change materials (PCM) containing carbon additives for heat storage application. *Int. J. Refrig.* 42, 112–120.
<https://doi.org/10.1016/j.ijrefrig.2014.02.004>
- Christian, H., Samarjit, C., Andreas, J., Markus, L., 2017. Phase Change Material in Battery Thermal Management Applications. *Tech. Univ. Munich* 152.
<https://mediatum.ub.tum.de/doc/1356376/1356376.pdf>
- Duan, J., Xiong, Y., Yang, D., 2019. Melting Behavior of Phase Change Material in Honeycomb Structures with Different Geometrical Cores. *Energies* 12, 2920.
<https://doi.org/10.3390/en12152920>
- Durakovic, B., Torlak, M., 2016. Experimental and numerical study of a PCM window model as a thermal energy storage unit. *Int. J. Low-Carbon Technol.* 12.
<https://doi.org/10.1093/ijlct/ctw024>
- Ed, V., John W., M., Justin, S., Xavier, P.-R., Tim, W., Adam, H., 2020. 15.3: Heat Capacity and Microscopic Changes [WWW Document]. *Chem. Libr.* URL
[https://chem.libretexts.org/Bookshelves/General_Chemistry/Book%3A_ChemPRIME_\(Moore_et_al.\)/15%3A_Thermodynamics-_Atoms_Molecules_and_Energy/15.03%3A_Heat_Capacity_and_Microscopic_Changes](https://chem.libretexts.org/Bookshelves/General_Chemistry/Book%3A_ChemPRIME_(Moore_et_al.)/15%3A_Thermodynamics-_Atoms_Molecules_and_Energy/15.03%3A_Heat_Capacity_and_Microscopic_Changes) (accessed 10.4.20).
- Fan, Y., Bao, Y., Ling, C., Chu, Y., Tan, X., Yang, S., 2019. Experimental study on the thermal management performance of air cooling for high energy density cylindrical

- lithium-ion batteries. *Appl. Therm. Eng.* 155, 96–109.
<https://doi.org/10.1016/j.applthermaleng.2019.03.157>
- Farid, M.M., Khudhair, A.M., Razack, S.A.K., Al-Hallaj, S., 2004. A review on phase change energy storage: materials and applications. *Energy Convers. Manag.* 45, 1597–1615.
<https://doi.org/10.1016/j.enconman.2003.09.015>
- Feng, X., Ouyang, M., Liu, X., Lu, L., Xia, Y., He, X., 2017. Thermal runaway mechanism of lithium ion battery for electric vehicles: A review. *Energy Storage Mater.* 10.
<https://doi.org/10.1016/j.ensm.2017.05.013>
- Fukai, J., Hamada, Y., Morozumi, Y., Miyatake, O., 2003. Improvement of thermal characteristics of latent heat thermal energy storage units using carbon-fiber brushes: Experiments and modeling. *Int. J. Heat Mass Transf.* 46, 4513–4525.
[https://doi.org/10.1016/S0017-9310\(03\)00290-4](https://doi.org/10.1016/S0017-9310(03)00290-4)
- Gaines, L., 2018. Lithium-ion battery recycling processes: Research towards a sustainable course. *Sustain. Mater. Technol.* 17, e00068.
<https://doi.org/10.1016/j.susmat.2018.e00068>
- Gümüŝsu, E., Ekici, Ö., Köksal, M., 2017. 3-D CFD modeling and experimental testing of thermal behavior of a Li-Ion battery. *Appl. Therm. Eng.* 120, 484–495.
<https://doi.org/10.1016/j.applthermaleng.2017.04.017>
- Hassan, A., Laghari, M., Rashid, Y., 2016. Micro-Encapsulated Phase Change Materials: A Review of Encapsulation, Safety and Thermal Characteristics. *Sustainability* 8, 1046.
<https://doi.org/10.3390/su8101046>
- Himran, S., Suwono, A., Mansoori, G.A., 1994. Characterization of Alkanes and Paraffin Waxes for Application as Phase Change Energy Storage Medium. *Energy Sources* 16, 117–128. <https://doi.org/10.1080/00908319408909065>

- I. Evans, T., E. White, R., 1989. A Thermal Analysis of a Spirally Wound Battery Using a Simple Mathematical Model. *J. Electrochem. Soc.* 136.
<https://doi.org/10.1149/1.2097230>
- Ianniciello, L., Biwolé, P.H., Achard, P., 2018. Electric vehicles batteries thermal management systems employing phase change materials. *J. Power Sources* 378, 383–403. <https://doi.org/10.1016/j.jpowsour.2017.12.071>
- International Energy Agency, 2020. Global electric car stock, 2010-2019 [WWW Document]. IEA. URL <https://www.iea.org/data-and-statistics/charts/global-electric-car-stock-2010-2019> (accessed 12.24.19).
- J. Willmott, C., Matsuura, K., 2005. Advantages of the Mean Absolute Error (MAE) over the Root Mean Square Error (RMSE) in Assessing Average Model Performance. *Clim. Res.* 30, 79. <https://doi.org/10.3354/cr030079>
- Joybari, M.M., Haghghat, F., Seddegh, S., Al-Abidi, A.A., 2017. Heat transfer enhancement of phase change materials by fins under simultaneous charging and discharging. *Energy Convers. Manag.* 152, 136–156.
<https://doi.org/10.1016/j.enconman.2017.09.018>
- Kim, S., Kim, H., 2016. A new metric of absolute percentage error for intermittent demand forecasts. *Int. J. Forecast.* 32, 669–679.
<https://doi.org/10.1016/j.ijforecast.2015.12.003>
- Kochhan, R., Fuchs, S., Reuter, B., Burda, P., Matz, S., Lienkamp, M., 2014. An Overview of Costs for Vehicle Components, Fuels and Greenhouse Gas Emissions.
https://www.researchgate.net/publication/260339436_An_Overview_of_Costs_for_Vehicle_Components_Fuels_and_Greenhouse_Gas_Emissions

- Kosky, P., Balmer, R., Keat, W., Wise, G., 2013. Chapter 12 - Mechanical Engineering, in: Kosky, P., Balmer, R., Keat, W., Wise, G. (Eds.), *Exploring Engineering* (Third Edition). Academic Press, Boston, pp. 259–281. <https://doi.org/10.1016/B978-0-12-415891-7.00012-1>
- Lai, Y., Wu, W., Chen, K., Wang, S., Xin, C., 2019. A compact and lightweight liquid-cooled thermal management solution for cylindrical lithium-ion power battery pack. *Int. J. Heat Mass Transf.* 144, 118581. <https://doi.org/10.1016/j.ijheatmasstransfer.2019.118581>
- Lambert, F., 2019. First look at Tesla's new V3 Supercharger in action. *Electrek*. URL <https://electrek.co/2019/03/07/tesla-v3-supercharger-action-first-look/> (accessed 8.2.20).
- Lauf, R.J., Hamby, C.J., 1990. Metallic phase-change materials for solar dynamic energy storage systems (No. ORNL/TM-11351). Oak Ridge National Lab., TN (USA). <https://doi.org/10.2172/6241485>
- Li, B., Zhai, X., 2017. Experimental investigation and theoretical analysis on a mid-temperature solar collector/storage system with composite PCM. *Appl. Therm. Eng.* 124, 34–43. <https://doi.org/10.1016/j.applthermaleng.2017.06.002>
- Lin, Y., Jia, Y., Alva, G., Fang, G., 2018. Review on thermal conductivity enhancement, thermal properties and applications of phase change materials in thermal energy storage. *Renew. Sustain. Energy Rev.* 82, 2730–2742. <https://doi.org/10.1016/j.rser.2017.10.002>
- Liu, G., Ouyang, M., Lu, L., Jianqiu, L., Han, X., 2014. Analysis of the heat generation of lithium-ion battery during charging and discharging considering different influencing factors. *J. Therm. Anal. Calorim.* 116. <https://doi.org/10.1007/s10973-013-3599-9>

- Ma, S., Jiang, M., Tao, P., Song, C., Wu, J., Wang, J., Deng, T., Shang, W., 2018. Temperature effect and thermal impact in lithium-ion batteries: A review. *Prog. Nat. Sci. Mater. Int.* 28, 653–666. <https://doi.org/10.1016/j.pnsc.2018.11.002>
- Mantilla Gilart, P., Yedra Martínez, Á., González Barriuso, M., Manteca Martínez, C., 2012. Development of PCM/carbon-based composite materials. *Sol. Energy Mater. Sol. Cells* 107, 205–211. <https://doi.org/10.1016/j.solmat.2012.06.014>
- Marques, L., Vasconcelos, V., Pereirinha, P.G., Trovão, J.P., 2011. Lithium Modular Battery Bank for Electric Vehicles. 12th Port.-Span. Conf. Electr. Eng. 5. https://www.uc.pt/en/efs/research/EESEVS/f/XIICLEEE_1846_MarquesEtAl.pdf
- Mathur, A., Kasetty, R., Oxley, J., Méndez, J.A., Nithyanandam, K., 2014. For SolarPACES 2013 USING ENCAPSULATED PHASE CHANGE SALTS FOR CONCENTRATED SOLAR POWER PLANT. <https://www.sciencedirect.com/science/article/pii/S1876610214005529>
- Maurizio, C., Giuseppina, C., Lo Brano, V., Marvuglia, A., Orioli, A., 2008. A Photovoltaic panel coupled with a phase changing material heat storage system in hot climates. pp. 1–13. https://www.researchgate.net/publication/233751432_A_Photovoltaic_panel_coupled_with_a_phase_changing_material_heat_storage_system_in_hot_climates
- May, M., 2018. Going electric: Here’s how much it actually costs to run an EV for a year [WWW Document]. *TheJournal.ie*. URL <https://www.thejournal.ie/how-much-does-it-cost-to-run-an-electric-car-4196606-Aug2018/> (accessed 9.28.20).
- Medved’, I., Trník, A., Vozár, L., 2016. Modeling of a heat capacity peak and an enthalpy jump for a paraffin-based phase-change material. https://www.researchgate.net/publication/307896586_Modeling_of_a_heat_capacity_peak_and_an_enthalpy_jump_for_a_paraffin-based_phase-change_material

- Mehling, H., Cabeza, L.F., 2008. Heat and cold storage with PCM: an up to date introduction into basics and applications ; with 28 tables, Heat and mass transfer. Springer, Berlin.
<https://www.springer.com/gp/book/9783540685562>
- Moghaddam, H., Mazyar, S., 2018. Designing battery thermal management systems (BTMS) for cylindrical Lithium-ion battery modules using CFD. <http://www.diva-portal.org/smash/get/diva2:1290856/FULLTEXT01.pdf>
- Newman, J., Tiedemann, W., 1995. Temperature Rise in a Battery Module with Constant Heat Generation. *J. Electrochem. Soc.* 142, 1054–1057.
<https://doi.org/10.1149/1.2044130>
- Nishi, Y., 2014. 2 - Past, Present and Future of Lithium-Ion Batteries: Can New Technologies Open up New Horizons?, in: Pistoia, G. (Ed.), *Lithium-Ion Batteries*. Elsevier, Amsterdam, pp. 21–39. <https://doi.org/10.1016/B978-0-444-59513-3.00002-9>
- OriginLab, 2019. Origin 2019B, Origin. OriginLab.
- Panchal, S., Mathewson, S., Fraser, R., Culham, R., Fowler, M., 2015. Thermal Management of Lithium-Ion Pouch Cell with Indirect Liquid Cooling using Dual Cold Plates Approach. *SAE Int. J. Altern. Powertrains* 4. <https://doi.org/10.4271/2015-01-1184>
- Pankaj, M., 2017. How a Car Air Conditioning System Works? - Nicely Explained. Mech. Boost. URL <https://www.mechanicalbooster.com/2017/12/car-air-conditioning-system.html> (accessed 10.3.20).
- Pesaran, A., Shriram, S., Gi-Heon, K., 2013. Addressing the Impact of Temperature Extremes on Large Format Li-Ion Batteries for Vehicle Applications.
<https://www.nrel.gov/docs/fy13osti/57747.pdf>
- Pincemin, S., Olives, R., Py, X., Christ, M., 2008. Highly conductive composites made of phase change materials and graphite for thermal storage. *Sol. Energy Mater. Sol. Cells* 92, 603–613. <https://doi.org/10.1016/j.solmat.2007.11.010>

- Quesnel, N., 2017. What Fluids Can Be Used With Liquid Cold Plates in Electronics Cooling Systems | Advanced Thermal Solutions [WWW Document]. URL <https://www.qats.com/cms/2017/11/13/fluids-can-used-liquid-cold-plates-electronics-cooling/> (accessed 2.2.20).
- Royal Society of Chemistry, 2020. Aluminium - Element information, properties and uses | Periodic Table [WWW Document]. R. Soc. Chem. URL <https://www.rsc.org/periodic-table/element/13/aluminium> (accessed 10.23.20).
- Salunkhe, P.B., Shembekar, P.S., 2012. A review on effect of phase change material encapsulation on the thermal performance of a system. *Renew. Sustain. Energy Rev.* 16, 5603–5616. <https://doi.org/10.1016/j.rser.2012.05.037>
- Sharma, A., Tyagi, V.V., Chen, C.R., Buddhi, D., 2009. Review on thermal energy storage with phase change materials and applications. *Renew. Sustain. Energy Rev.* 13, 318–345. <https://doi.org/10.1016/j.rser.2007.10.005>
- SIEMENS, 2019. How to link an electric vehicle battery cooling system with the air conditioning system [WWW Document]. URL <https://community.sw.siemens.com/s/article/how-to-link-an-electric-vehicle-battery-cooling-system-with-the-air-conditioning-system> (accessed 1.21.20).
- Singh, R., Sadeghi, S., Shabani, B., 2019. Thermal Conductivity Enhancement of Phase Change Materials for Low-Temperature Thermal Energy Storage Applications. *Energies* 12, 75. <https://doi.org/10.3390/en12010075>
- Sundin, D.D., 2018. Mineral Oil and Corrosive Sulfur: What is eating away at your immersed electronics? [WWW Document]. *engineeredfluids2018*. URL <https://www.engineeredfluids.com/post/mineral-oil-and-corrosive-sulfur-what-is-eating-away-at-your-immersed-electronics> (accessed 10.3.20).

- Sundin, D.W., Sponholtz, S., 2020. Thermal Management of Li-Ion Batteries With Single-Phase Liquid Immersion Cooling. *IEEE Open J. Veh. Technol.* 1, 82–92.
<https://doi.org/10.1109/OJVT.2020.2972541>
- U.S. Energy Information Administration, 2016. Transportation sector energy consumption.
<https://www.eia.gov/outlooks/ieo/pdf/transportation.pdf>
- Valavanidis, A., 2018. The Shift to Diesel Fuel Engines and How the Emission Scandal of Diesel Vehicles Unfolded. *World Energy Consumption of Transportation Sector 1*, 1–26.
https://www.researchgate.net/publication/322926517_The_Shift_to_Diesel_Fuel_Engines_and_How_the_Emission_Scandal_of_Diesel_Vehicles_Unfolded_World_Energy_Consumption_of_Transportation_Sector
- Wang, J., Xie, H., Xin, Z., 2009. Thermal properties of paraffin based composites containing multi-walled carbon nanotubes. *Thermochim. Acta* 488, 39–42.
<https://doi.org/10.1016/j.tca.2009.01.022>
- Wang, Z., Zhang, Y., Liu, J., 2015. Comparison between five typical reinforced honeycomb structures. *5th Int. Conf. Adv. Eng. Mater. Technol. AEMT 2015*.
<https://doi.org/10.2991/icaemt-15.2015.134>
- Wiebelt, Dr.-I., Heckenberger, Dr.-I., 2010. Integration of a Lithium-Ion Battery Into Hybrid and Electric Vehicles. *ATZautotechnology* 10. <https://doi.org/10.1007/BF03247161>
- Xia, G., Cao, L., Bi, G., 2017. A review on battery thermal management in electric vehicle application. *J. Power Sources* 367, 90–105.
<https://doi.org/10.1016/j.jpowsour.2017.09.046>
- Xinran, T., J., W., 2014. Cooling Air Temperature and Mass Flow Rate Control for Hybrid Electric Vehicle Battery Thermal Management. *Proc. ASME 2014 Dyn. Syst. Control Conf.* <https://doi.org/10.1115/DSCC2014-6001>

Zhang, G., Cao, L., Ge, S., Wang, C.-Y., Shaffer, C.E., Rahn, C.D., 2014. In Situ Measurement of Radial Temperature Distributions in Cylindrical Li-Ion Cells. J. Electrochem. Soc. 161, A1499–A1507. <https://doi.org/10.1149/2.0051410jes>

Zivkovic, B., Fujii, I., 2001. An analysis of isothermal phase change of phase change material within rectangular and cylindrical containers. Sol. Energy 70, 51–61. [https://doi.org/10.1016/S0038-092X\(00\)00112-2](https://doi.org/10.1016/S0038-092X(00)00112-2)

8. Bibliography

Hwang, F., Confrey, T., Scully, S., Callaghan, D., Nolan, C., Kent, N. and Flannery, B., 2020. MODULAR PHASE CHANGE MATERIAL (PCM) THERMAL MANAGEMENT SYSTEMS FOR CYLINDRICAL LI-ION CELLS. Proceeding of 5th Thermal and Fluids Engineering Conference (TFEC), New Orleans, LA, USA

Hwang, F., Confrey, T., Scully, S., Callaghan, D., Nolan, C., Kent, N. and Flannery, B., 2020. MODELLING OF HEAT GENERATION IN AN 18650 LITHIUM-ION BATTERY CELL UNDER VARYING DISCHARGE RATES. Proceeding of 5th Thermal and Fluids Engineering Conference (TFEC), New Orleans, LA, USA

Hwang, F., Confrey, T., Scully, S.. Fin embedded composite PCM thermal management system for EV. Environ 2019 29th Irish Environmental Researchers Colloquium, Carlow, Ireland

9. Appendices

```

/*****
UDF for time dependent volumetric heat generation of 18650 cell 0.5C Discharge
Polynomial Function
*****/
#include "udf.h"
#define C1 2.08421E-20 //define constant term
#define C2 -4.76532E-16
#define C3 4.28892E-12
#define C4 -1.9141E-8
#define C5 4.38744E-5
#define C6 -0.0479
#define C7 16.87801
#define C8 21712.10211

DEFINE_SOURCE(heat_gen, cell, thread, dS, eqn)
{
    real source;
    real time;
    time = CURRENT_TIME; //taking time value;

    source = C1 * pow(time, 7) + C2 * pow(time, 6) + C3 * pow(time, 5) + C4 *
pow(time, 4) + C5 * pow(time, 3) + C6 * pow(time, 2) + time * C7 + C8; //time
dependent heat source;
    dS[eqn] = 0;
    return source;
}

/*****
UDF for time dependent volumetric heat generation of 18650 cell 1C Discharge
Polynomial Function
*****/
#include "udf.h"
#define C1 5.30808E-18 //define constant term
#define C2 -6.46039E-14
#define C3 3.1209E-10
#define C4 -7.57977E-7
#define C5 9.682E-4
#define C6 -0.61572
#define C7 152.02273
#define C8 57681.93928

DEFINE_SOURCE(heat_gen, cell, thread, dS, eqn)
{
    real source;
    real time;
    time = CURRENT_TIME; //taking time value;

    source = C1 * pow(time, 7) + C2 * pow(time, 6) + C3 * pow(time, 5) + C4 *
pow(time, 4) + C5 * pow(time, 3) + C6 * pow(time, 2) + time * C7 + C8; //time
dependent heat source;
    dS[eqn] = 0;
    return source;
}

```

```

/*****
UDF for time dependent volumetric heat generation of 18650 cell 1.5C Discharge
Polynomial Function
*****/
#include "udf.h"
#define C1 1.76047E-16 //define constant term
#define C2 -1.44892E-12
#define C3 4.72336E-9
#define C4 -7.73246E-6
#define C5 0.00665
#define C6 -2.83586
#define C7 465.10366
#define C8 119986.99372

DEFINE_SOURCE(heat_gen, cell, thread, dS, eqn)
{
    real source;
    real time;
    time = CURRENT_TIME; //taking time value;

    source = C1 * pow(time, 7) + C2 * pow(time, 6) + C3 * pow(time, 5) + C4 *
pow(time, 4) + C5 * pow(time, 3) + C6 * pow(time, 2) + time * C7 + C8; //time
dependent heat source;
    dS[eqn] = 0;
    return source;
}

/*****
UDF for time dependent volumetric heat generation of 18650 cell 2C Discharge
Polynomial Function
*****/
#include "udf.h"
#define C1 1.1448E-15 //define constant term
#define C2 -7.0640037800995E-12
#define C3 1.74347E-8
#define C4 -2.19104E-5
#define C5 0.014732786
#define C6 -5.023139503
#define C7 677.5244696
#define C8 155972.203

DEFINE_SOURCE(heat_gen, cell, thread, dS, eqn)
{
    real source;
    real time;
    time = CURRENT_TIME; //taking time value;

    source = C1 * pow(time, 7) + C2 * pow(time, 6) + C3 * pow(time, 5) + C4 *
pow(time, 4) + C5 * pow(time, 3) + C6 * pow(time, 2) + time * C7 + C8; //time
dependent heat source;
    dS[eqn] = 0;
    return source;
}

```

```

/*****
UDF for time dependent volumetric heat generation of 18650 cell 3C Discharge
Polynomial Function
*****/
#include "udf.h"
#define C1 1.16088E-14 //define constant term
#define C2 -4.70962E-11
#define C3 7.58379E-8
#define C4 -6.13961E-5
#define C5 0.02614
#define C6 -5.54148
#define C7 456.06819
#define C8 257681.93928

DEFINE_SOURCE(heat_gen, cell, thread, dS, eqn)
{
    real source;
    real time;
    time = CURRENT_TIME; //taking time value;

    source = C1 * pow(time, 7) + C2 * pow(time, 6) + C3 * pow(time, 5) + C4 *
pow(time, 4) + C5 * pow(time, 3) + C6 * pow(time, 2) + time * C7 + C8; //time
dependent heat source;
    dS[eqn] = 0;
    return source;
}

```

```

/*****
UDF for time dependent volumetric heat generation of 18650 cell 1C Discharge Power
Function
*****/
#include "udf.h"
#define Q0 55107.37895 //define constant term
#define A 1.15056E-17
#define xc 1481.83901
#define P 6.58794

DEFINE_SOURCE(heat_gen, cell, thread, dS, eqn)
{
    real source;
    real time;
    time = CURRENT_TIME; //taking time value;

    source = Q0 + A * pow(abs(time - xc), P); //time dependent heat source;
    dS[eqn] = 0;
    return source;
}

```

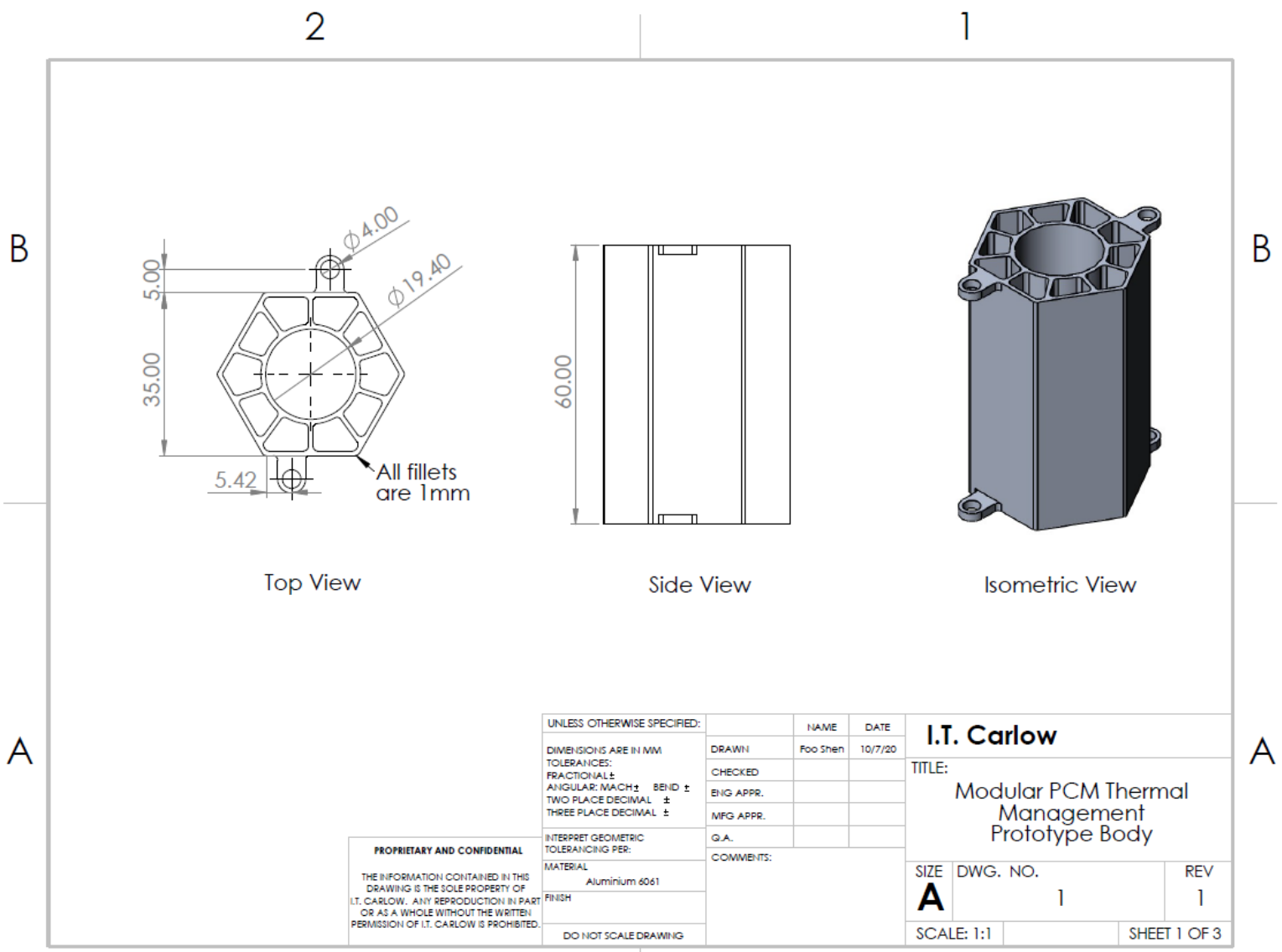
```

/*****
UDF for time dependent volumetric heat generation of 18650 cell Discharge Exponential
Function
*****/
#include "udf.h"
#define Q0 63518.40155 //define constant term
#define A1 104.63607
#define t1 478.017
#define A2 -1833.72011
#define t2 879.11626

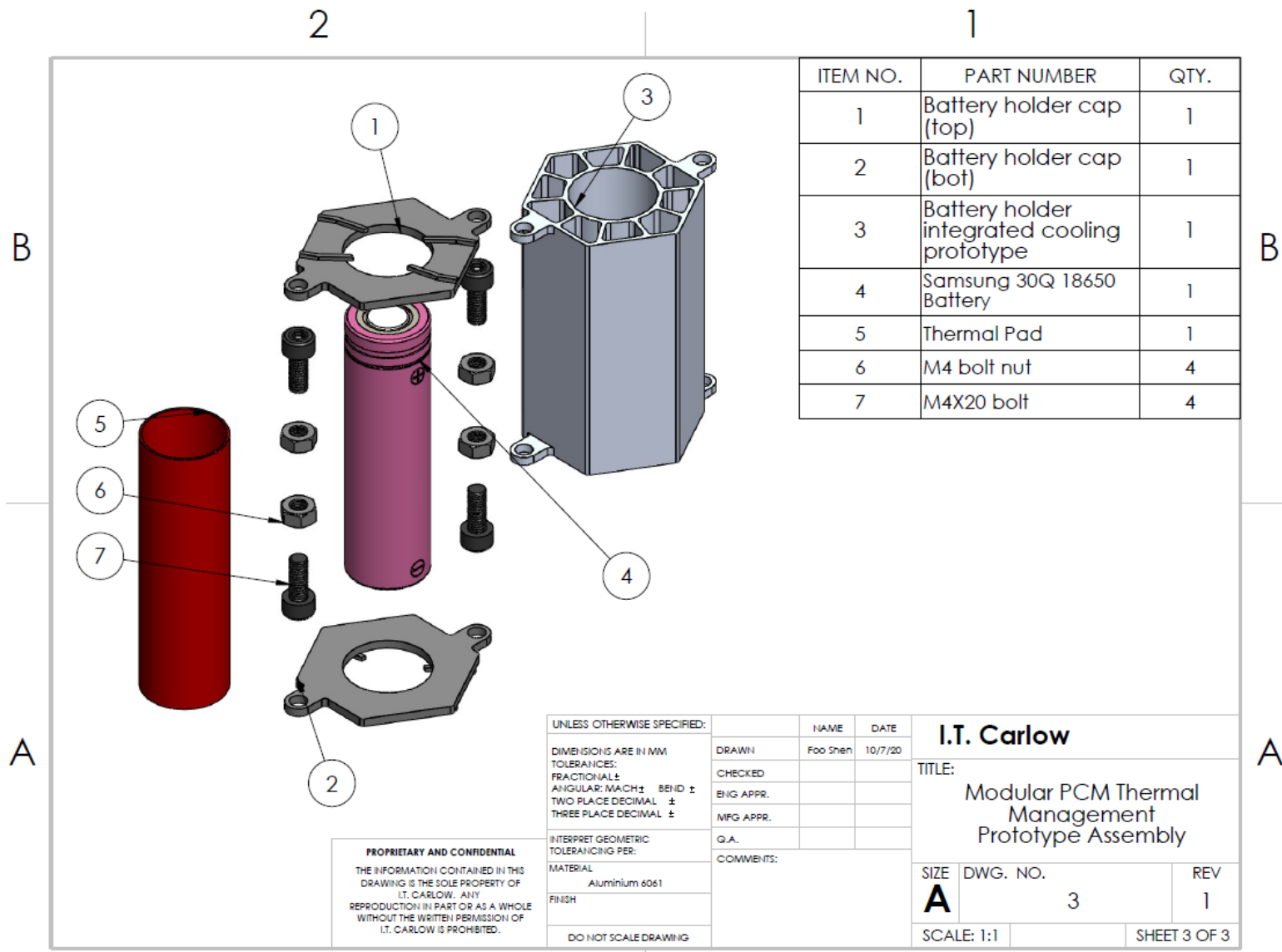
```

```
DEFINE_SOURCE(heat_gen, cell, thread, dS, eqn)
{
    real source;
    real time;
    time = CURRENT_TIME; //taking time value;

    source = A1 * exp(time/t1) + A2 * exp(time/t2) + Q0; //time dependent heat
source;
    dS[eqn] = 0;
    return source;
}
```



SOLIDWORKS Educational Product. For Instructional Use Only.



ITEM NO.	PART NUMBER	QTY.
1	Battery holder cap (top)	1
2	Battery holder cap (bot)	1
3	Battery holder integrated cooling prototype	1
4	Samsung 30Q 18650 Battery	1
5	Thermal Pad	1
6	M4 bolt nut	4
7	M4X20 bolt	4

UNLESS OTHERWISE SPECIFIED:	NAME	DATE
DIMENSIONS ARE IN MM	DRAWN	10/7/20
TOLERANCES:	CHECKED	
FRACTIONAL ±	ENG APPR.	
ANGULAR: MACH ± BEND ±	MFG APPR.	
TWO PLACE DECIMAL ±	Q.A.	
THREE PLACE DECIMAL ±	COMMENTS:	
INTERPRET GEOMETRIC TOLERANCING PER:		
MATERIAL		
Aluminium 6061		
FINISH		
DO NOT SCALE DRAWING		

PROPRIETARY AND CONFIDENTIAL
 THE INFORMATION CONTAINED IN THIS DRAWING IS THE SOLE PROPERTY OF I.T. CARLOW. ANY REPRODUCTION IN PART OR AS A WHOLE WITHOUT THE WRITTEN PERMISSION OF I.T. CARLOW IS PROHIBITED.

I.T. Carlow		
TITLE: Modular PCM Thermal Management Prototype Assembly		
SIZE A	DWG. NO. 3	REV 1
SCALE: 1:1		SHEET 3 OF 3

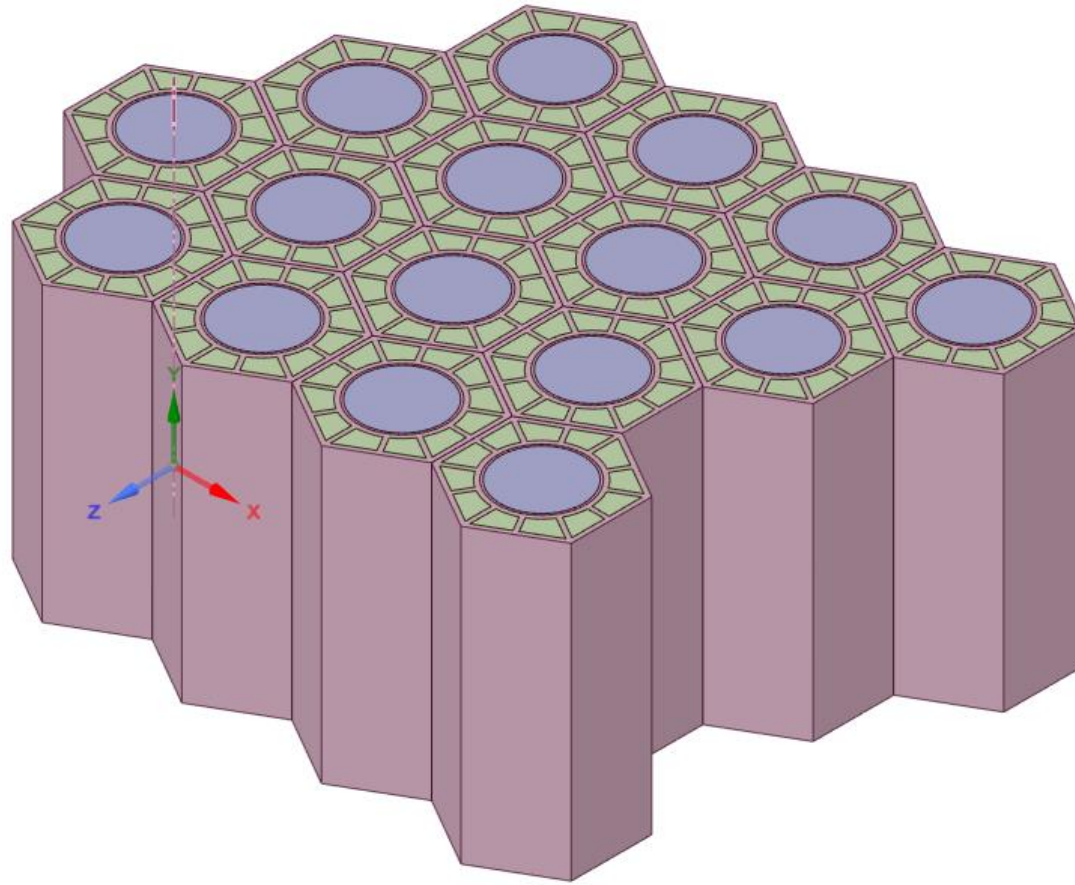


Fig. 49 Sixteen cell prototype assembly

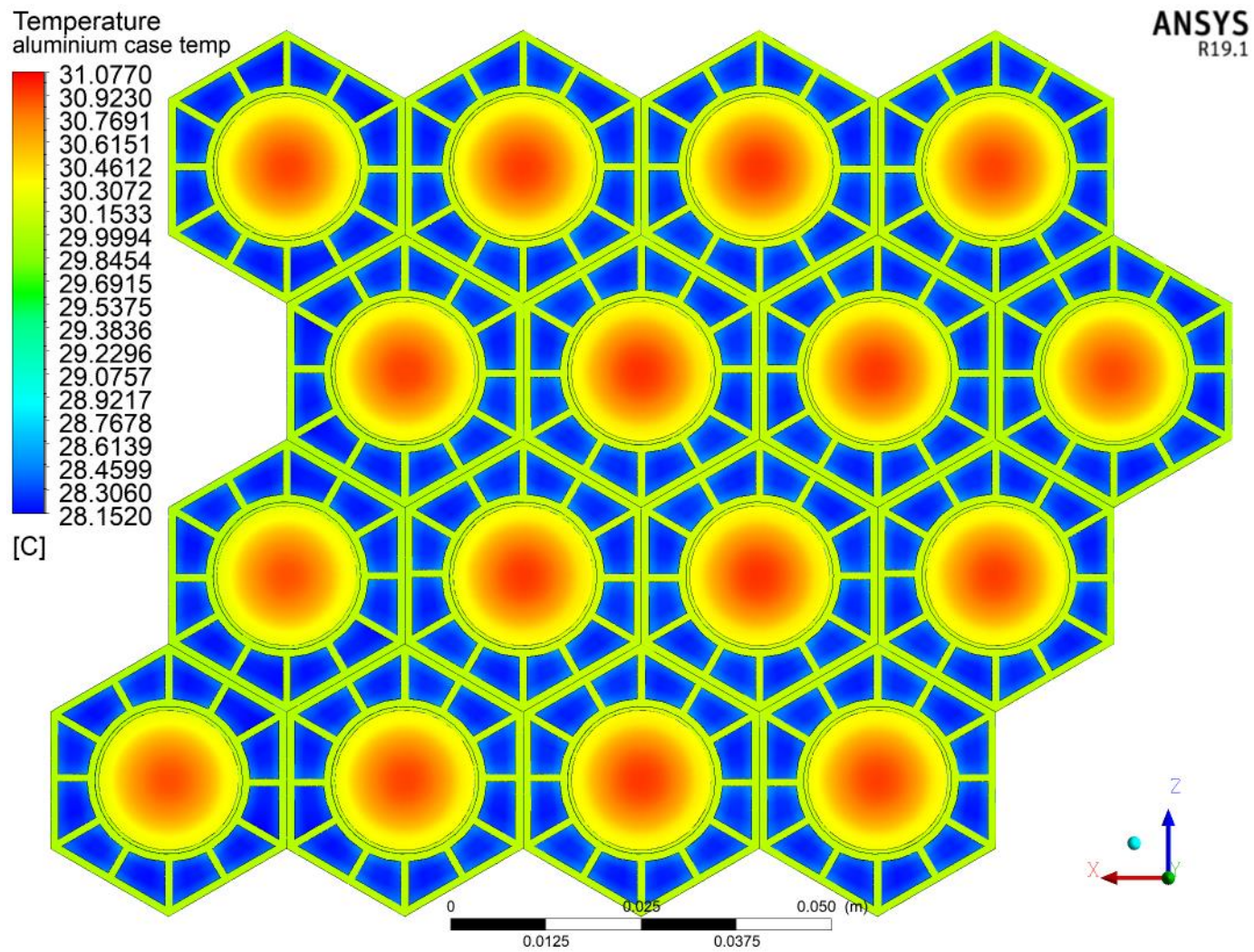


Fig. 50 1.00C discharge of the 16-cell prototype after a duration 3600s